Hybrid Integrated Ultra-Broadband Optical Receiver for Radio-over-Fiber Application

Chih-Wang Young

A Thesis

In the Department

of

Electrical and Computer Engineering

Presented in Partial Fulfillment of the Requirements

For the Degree of Master of Applied Science at

Concordia University

Montréal, Québec, Canada

November 2012

© Chih-Wang Young, 2012

CONCORDIA UNIVERSITY

School of Graduate Studies

This is to certify that the thesis prepared

By: Chih-Wang Young I.D. 9471138

Entitled: Hybrid Integrated Ultra-Broadband Optical Receiver for Radio-over-Fiber Application

and submitted in partial fulfillment of the requirements for the degree of

Master of Applied Science

complies with the regulations of the University and meets the accepted standards with respect to originality and quality.

Signed by the final examining committee:

____ Chair

____ Examiner

____ Examiner

____ Supervisor

Approved by ____

Chair of Department or Graduate Program Director

____

Dean of Faculty

Date ____

ABSTRACT

Hybrid Integrated Ultra-Broadband Optical Receiver

for Radio-over-Fiber Application

Chih-Wang Young

Communication is an integral part of people's daily life, and its demand will never cease. After multiple generations of communication system improvement, broadband wireless communication has become a conspicuous development trend but the congested spectrum has turned into one of the system bottlenecks. Therefore, shifting into higher frequency bands, that is, wavelengths of millimeter scale would be a solution to suffice the escalating consumer demand, and Radio-over-Fiber (RoF) is the key for successful system deployment. Under RoF structure, Radio Frequency (RF) signals can be directly distributed from central station to base stations via optical fiber, as a result, size of base station can be implemented into a palm-size package, and more importantly, lower unit cost of base stations crucial due to high volume use.

In this work, we started with the design of an optical receiver as the first step of transceiver integration, and targeted at 40 GHz or above. Different from the widespread

digital optical receiver, optical nature of RoF transmission is analog signal, and consequently its receiver demands higher qualification standards. Noise, intermodulation distortion, nonlinearities and other aspects are all required to be validated.

Putting the cost factor into consideration, we used Miniature Hybrid Microwave Integrated Circuit (MHMIC) technology to implement our analog optical receiver. Design and simulation of the 40 GHz receiver was mainly carried out by Agilent Advanced Design System (ADS), and the bondwire interconnection is identified as a major potential bandwidth degradation factor of the receiver.

After the circuit fabrication, the S-parameter results showed the receiver bandwidth is limited to 30 GHz due to certain fabrication error caused by bondwires. The bandwidth evaluation is further verified from Error Vector Magnitude (EVM) results by transmitting Ultra-wideband (UWB) signal centered at 30.31 GHz through a 20 KM long optical fiber. In back-to-back characterization of the receiver, the 1-dB compression point is found as 11.7 dBm (referred to input) and the SFDR based on two sets of two-tone frequencies (4 GHz with 6 GHz, and 13 GHz with 14 GHz) is 107.45 dB/Hz$^{2/3}$. Responsivity of the receiver is 0.325 A/W at 1550 nm.

ACKNOWLEDGMENTS

I would like to present my gratitude to my supervisor Dr. X. Zhang, for giving me this opportunity to learn and to challenge myself. I would like to thank Dr. B. Hraimel, for bringing me inspirations and tolerating my endless disputes. I would also like to thank Mr. J. Gauthier and Mr. T. Antonescu for their technical assistance on circuit fabrication.

During off-campus measurement, I am really grateful for Mr. Meer Sakib, PhD candidate from McGill University, for squeezing his already-busy-time out to assist me. I am also grateful for Mr. David Dousset from École Polytechnique de Montréal, for answering and arranging my continuous request for all kinds of equipments.

Last but not the least, I would like to thank my parents for their understanding and support, because I will never made it this far without them.

TABLE OF CONTENTS

List of Figures ix

List of Tables xiv

List of Acronyms xv

List of Principal Symbols xvii

Chapter 1: Introduction 1

1.1 Technology Review 1

1.1.1 Millimeter-wave Communication 1

1.1.2 Radio-over-Fiber 2

1.1.3 Optical Transceiver 4

1.2 Related Works and Motivation 6

1.3 Thesis Contribution 9

1.4 Thesis Outline 10

Chapter 2: Design and Analysis 11

2.1 Introduction 11

2.2 Optical Components 13

2.2.1 Lensed Fiber 13

2.2.2 Photodetector 16

2.3 Electrical Components 24

2.3.1 Transimpedance Amplifier 24

2.3.2 Interconnection 32

2.3.3 Output Transmission Line 37

2.3.4 DC Bias Circuit 50

2.4 Summary 53

Chapter 3: Circuit Simulation 54

3.1 Introduction 54

3.2 S-Parameter and Group Delay 55

3.3 Items bypassed 58

3.3.1 Potential Degradation Factors 59

3.3.2 Simulation Analysis 59

3.4 Summary 60

Chapter 4: Experimental Characterization 61

4.1 Introduction 61

4.2 Circuit Fabrication 62

4.3 Circuit Characterization 68

4.3.1 Responsivity 68

4.3.2 S-Parameter and Group Delay 70

4.3.3 Error Vector Magnitude 75

4.3.4 Dynamic Range 80

4.3.5 Eye-Diagram 87

4.4 Summary 91

Chapter 5: Conclusion 93

5.1 Concluding Remarks 93

5.2 Future Work 95

Bibliography 98

LIST OF FIGURES

Figure 1.1: Basic architecture of RoF. 3

Figure 1.2: Block diagram of optical transceiver 5

Figure 2.1: Conventional optical coupling structure. 14

Figure 2.2: Optical coupling structure simplified by using lensed fiber. 14

Figure 2.3: Light intensity distribution in optical fiber. 15

Figure 2.4: Schematic of surface-illuminated photodetector. 17

Figure 2.5: Schematic of side-illuminated photodetector. 18

Figure 2.6: Layout and physical dimension of Archcom AC6180. 22

Figure 2.7: Simulation model of PD AC6180 in ADS. 23

Figure 2.8: Estimated frequency response of PD AC6180. 24

Figure 2.9: Basic schematic of shunt-feedback amplifier 25

Figure 2.10: Layout of TIA 4335TA. 29

Figure 2.11: S-parameter of TIA 4335TA. 30

Figure 2.12: Schematic of output transmission line with V-connectors. 31

Figure 2.13: Interconnection gaps among PD, TIA, and output transmission line. 34

Figure 2.14: 3D model of bondwire simulated. 35

Figure 2.15: Bondwire insertion loss at different length and height. 36

Figure 2.16: (a) Conductor-Backed Coplanar Waveguide (b) Microstrip line. 39

Figure 2.17: CPW inductor. 42

Figure 2.18: S_{21} of CPW inductor in different sizes. 44

Figure 2.19: Microstrip spiral inductor 45

Figure 2.20: S_{21} of microstrip inductor in different sizes. 47

Figure 2.21: Insertion Loss of RF Inductor BCR-122 and RF Capacitor GX02............. 48

Figure 2.22: Main circuit final layout and area indicators 49

Figure 2.23: Close view of PD and TIA layout 50

Figure 2.24: DC bias circuit for TIA and PD. 51

Figure 2.25: Layout of DC bias circuit. 52

Figure 3.1: Schematic of the optical receiver. 55

Figure 3.2: S-parameter of the final circuit with different bondwire lengths. 56

Figure 3.3: Group delay of long/short bondwire configuration 58

Figure 4.1: Final product of the optical receiver module. 63

Figure 4.2: Possible RF feedback loop. 64

Figure 4.3: Circuit close view after the installation of lensed fiber. 66

Figure 4.4: Close view of circuit core components. 67

Figure 4.5: Setup for responsivity measurement 69

Figure 4.6: Responsivity of optical receiver. 70

Figure 4.7: Setup for S-parameter measurement. 71

Figure 4.8: S_{21} response of the reference circuit and the optical receiver module. 72

Figure 4.9: S_{21} response of the bias-tee from Picosecond Pulse Labs. 73

Figure 4.10: Compensated S_{21} of the optical receiver. 74

Figure 4.11: Group delay of the optical receiver. 75

Figure 4.12: Spectrum allocation of WiMedia UWB.. 76

Figure 4.13: Setup for EVM measurement.. 77

Figure 4.14: Electrical spectrum of up-converted UWB at the optical receiver. 79

Figure 4.15: RF input power versus EVM and constellation at lowest EVM point........ 80

Figure 4.16: Setup for dynamic range measurement... 81

Figure 4.17: RF input power versus output gain at different frequencies....................... 83

Figure 4.18: 1-dB compression point referred to RF input. 83

Figure 4.19: SFDR of the first set signal... 84

Figure 4.20: SFDR of the second set signal. 85

Figure 4.21: Output power of the first set signal and IMD3 86

Figure 4.22: Output power of the second set signal and IMD3....................................... 86

Figure 4.23: Setup for eye-diagram measurement. 88

Figure 4.24: Eye-diagram at 12 Gbps.. 89

Figure 4.25: Eye-diagram at 40 Gbps.. 90

Figure 4.26: Eye-diagram at 43 Gbps.. 91

LIST OF TABLES

Table 1-1: Parameters of different optical receivers. 9

Table 2-1: Main PD specifications from Archcom and Enablence. 21

Table 2-2: Electrical specifications of different TIAs. 28

Table 2-3: Summary of bondwire parameters. 35

Table 2-4: Geometrical dimensions of CPW inductor. 43

Table 2-5: Geometrical dimensions of microstrip inductor. 46

Table 2-6: Component specifications of DC bias circuit. 51

Table 3-1: Simulation result of final circuit S-parameter. 57

List of Acronyms

ADS	Advanced System Design
BER	Bit Error Rate
CDR	Clock and Data Recovery
CML	Current Mode Logic
CPW	Coplanar Waveguide
EDFA	Erbium Doped Fiber Amplifier
EVM	Error Vector Magnitude
FWHM	Full-Width-at-Half-Maximum
IMD3	Third-order Intermodulation
LD	Laser Diode
MFD	Mode-Field Diameter
MHMIC	Miniature Hybrid Microwave Integrated Circuit
MMIC	Monolithic Microwave Integrated Circuit
MMW	Millimeter-wave
MZM	Mach-Zehnder Modulator
OFDM	Orthogonal Frequency-Division Multiplexing

OOK	On-Off Keying
PCB	Print Circuit Board
PD	Photodetector
RF	Radio Frequency
RoF	Radio-over-Fiber
SA	Signal Analyzer
SFDR	Spurious-Free Dynamic Range
SMF	Single-Mode Fiber
SMT	Surface-Mount Technology
TIA	Transimpedance Amplifier
TOI	Third-Order Intercept point
UWB	Ultra-Wideband
VNA	Vector Network Analyzer

LIST OF PRINCIPAL SYMBOLS

A/W	Ampere per Watt, responsivity of the photodetector
h	Planck constant, 6.626×10^{-34} J·s
q	Elementary charge, 1.602×10^{-19} Coulombs
V/W	Volts per Watt, conversion gain from optical to electrical

CHAPTER 1: INTRODUCTION

1.1 Technology Review

1.1.1 Millimeter-wave Communication

With the increasing demand of broadband service for wireless and fixed terminals, it had led to the consideration of seeking alternative frequency bands among the congested radio spectrum, especially into higher frequency bands. In recent times, Millimeter-Wave (MMW) frequency bands (30 GHz to 300 GHz) are gaining more attention because of the capacity to provide gigabit scale data rates by taking the full advantage of the vast bandwidth presented.

Local Multipoint Distribution Service (LMDS) is one of the wireless access technologies that operate on MMW frequencies across 26 GHz and 31.3 GHz. It was originally designed for the distribution of digital television transmission, but later it is also used as an interconnection media among high-traffic network. Aside from LMDS frequency bands, many other MMW bands are already reserved for future wireless services that are still developing [1].

On the other hand, terrestrial MMW signals are subject to atmospheric attenuation, particularly from 57 GHz to 67 GHz. Hence, the coverage distance of MMW transmission is basically limited to line-of-sight communication. It may be seen as an adverse at first, but on the contrary, this may turn into its own advantage because of high frequency reusability provided the short transmission range, and overall characterizing the system with better spectrum efficiency. This coverage area limitation can be overcome by deploying multiple microcell or picocell stations, predominantly in metropolitan areas because of high user concentration, such as airport, shopping center, metro station, and indoor building.

1.1.2 Radio-over-Fiber

As a consequence of deploying large amount of base stations, the system will need a high capacity interconnection platform as well as inexpensive base stations due to the high volume involved, and Radio-over-Fiber (RoF) technology is one of the most prominent solutions to transport and distribute radio frequency signals efficiently and economically.

Apart from those well-known advantages of optical fiber, such as broad bandwidth, low loss and immune to electromagnetic interference, RoF technology features with slim

system architecture that is mainly manifested on its remote stations, which implies lower construction cost and higher deployment flexibility. Other benefits of RoF are centralized control and upgrade, dynamic radio resource configuration and capacity allocation, minimized multi-path effects and others [2].

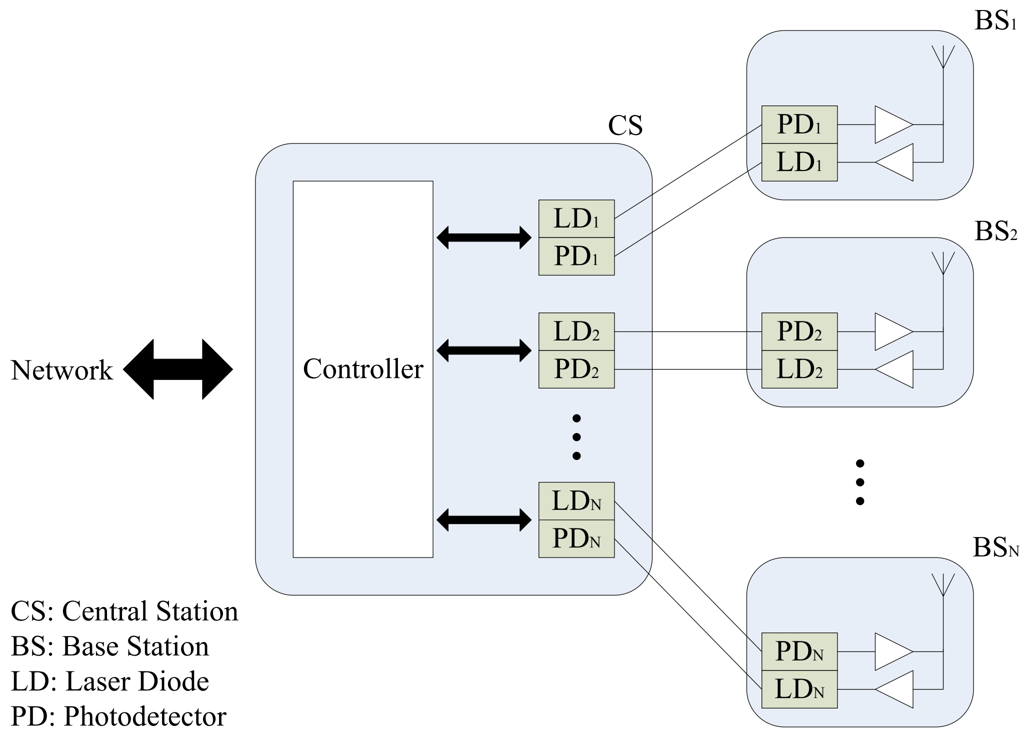

Figure 1.1: Basic architecture of RoF.

In RoF system, as shown is Figure 1.1, neither upscale nor downscale of electrical signals are needed at BSs because they are already handled by the CS, including signal coding, modulation and multiplexing. Under this scenario, RF signals are directly

uploaded to the communication link, and as a result, size and power consumption of BSs are considerably reduced.

Unlike the widespread digital optical fiber communication, i.e. gigabit Ethernet or mainstream fiber transmission links of base stations, RoF is an analog transmission system in nature, since radio waveforms are directly distributed from CS to BS at radio carrier frequency. This fundamental nature might reduce the resistance of RoF against impairments such as noise or distortion, resulting more rigorous standards comparing to its digital counterpart. But despite this fact, RoF has still emerged in recent years because of its competence in satisfying the growing consumer demand for broadband services.

An application example of RoF system is the wireless service established during the 2000 Sydney Olympic Games. Over 500 remote antennas were deployed in the area, handling calls from three GSM operators at different frequencies (900 MHz and 1800 MHz), and some BS used is just of a palm size [3].

1.1.3 Optical Transceiver

To better understand the optical communication system, essential components of an optical transceiver are shown in Figure 1.2. On the transmitter side, electrical signal prior

modulation is processed by a Digital Logic, it may include data multiplexing, encryption, error-correcting code insertion or others. Under direct modulation scheme, the Driver directly modulates the driving current of the Laser Diode (LD), and then the modulated signal is coupled into the fiber.

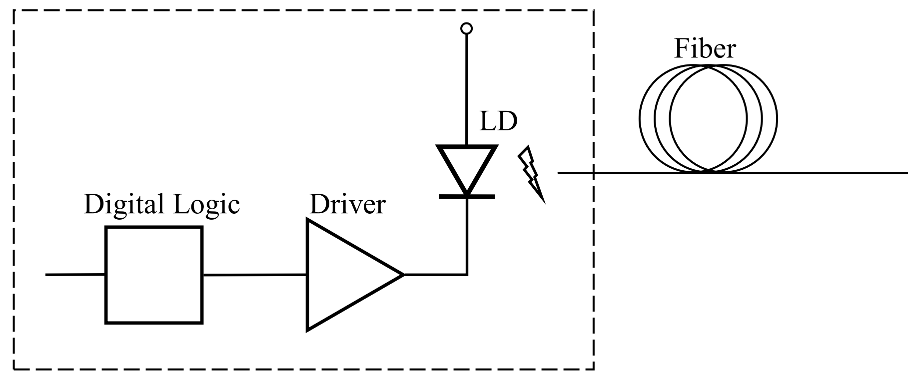

(a) Optical transmitter

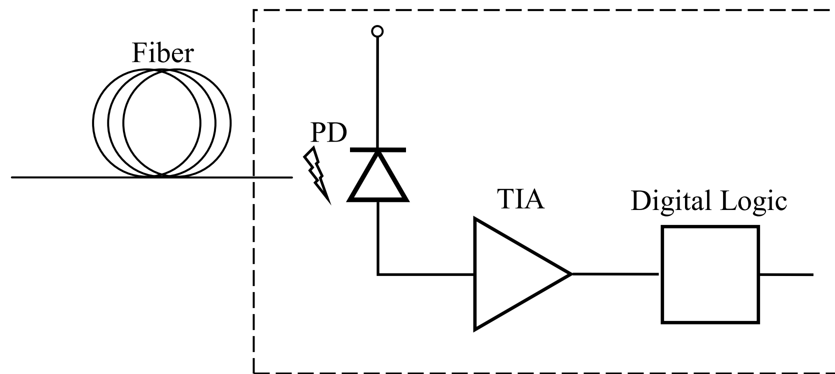

(b) Optical receiver

Figure 1.2: Block diagram of optical transceiver

At the receiver end, the optical pulse is converted into electrical current by a Photodetector (PD), and then first level amplification and current-to-voltage conversion

are carried out simultaneously by the Transimpedance Amplifier (TIA). An additional amplifier shall be added when the output voltage is found insufficient to drive the following stage, otherwise the signal could be fed into the Digital Logic for Clock and Data Recovery (CDR), demultiplexing, error checks and other tasks. In case of RoF optical receiver, TIA's output will be connected to a RF amplifier and subsequently broadcasting the RF signal via antenna.

As the first step toward the fully integration of optical transmitter and receiver for RoF application, we have decided to start with the design of a receiver before further integration.

1.2 Related Works and Motivation

In the evaluation of digital optical receiver, it generally engages three key indicators: bandwidth, conversion gain, and sensitivity. But unlike the digital optical link, the analog nature of RoF composes its modules with higher specification requirements than digital system. In addition to those indicators previously stated, dynamic range, intermodulation distortion, noise susceptibility, all these aspects should be assessed for a RoF optical receiver.

In the work presented by A.K. Dutta et al. in [4], they have demonstrated a hybrid integrated 40 Gbps digital optic link front-end, featuring with -5.8 dBm sensitivity at BER = 10^{-9}, and its conversion gain is 112 V/W. Later in [5], Y. Kwon et al. have presented another design of similar performance and fabrication technology, but features with improved optical coupling structure leading to higher sensitivity. This improvement was achieved by integrating a spot-size converter between the optical fiber and the PD, for the purpose of reducing the mode-size mismatch, and the sensitivity reached -11 dBm at BER = 10^{-10}. Commercialized 40 Gbps optical receivers are also available. SHF Communication Technologies AG has launched an Optical-to-Electrical Conversion Module [6] with improved conversion gain comparing to those listed above, it ranges between 350 V/W to 450 V/W. However, its sensitivity remains as a typical value of -9 dBm with BER = 10^{-10}. Despite the fact of various 40 GHz range optical receiver, their quality on delivering analog optical signal remained unknown since most of the essential parameters of analog optic were not provided or even analyzed.

As an optical receiver of RoF system, wider bandwidth is always desirable for its capacity of handling more radio spectrum signals. As stated before, from FCC current spectrum allocation, there are several frequency bands between 25 GHz and 50 GHz

proposed for future wireless services. Besides of the bandwidth, fabrication cost is also a critical factor always to be included. The manufacturing process of the receiver circuit is a task with high degree of freedom, allowing the designer to optimize in different approaches. There are works implemented in different technologies such as CMOS process, or in traditional microwave circuit fabrication technology plus other additional procedures like micromachining, or thin-film insertion. Nevertheless, the association with advanced fabrication process or multiple procedures may overreach the baseline of cost factor, which is a non-negligible part of RoF technology.

Based on these reasons, we have targeted to implement an analog optical receiver of 40 GHz or plus at minimum cost, and, with a complete analysis of analog aspects for RoF optical receiver, because to the best of our knowledge, no work has done so far for MMW analog optical receiver of this frequency range. Estimated performance parameters are summarized in Table 1-1 along with all works previously mentioned.

Works	Bandwidth	Gain	Sensitivity
[4]	45 GHz	112 V/W	-5.8 dBm @ BER=10^{-9}
[5]	40 GHz	N/A	-11 dBm @ BER = 10^{-10}
[6]	30 GHz	450 V/W	-9 dBm @ BER = 10^{-10}
Goal	40 GHz +	255 V/W	-9 dBm @ BER = 10^{-12}

Table 1-1: Parameters of different optical receivers.

1.3 Thesis Contribution

In this thesis we have developed a broadband optical receiver module as part of the RoF application, and main contributions can be summarized as follows:

- Design, implementation and characterization of an optical receiver for analog optical link application, targeted at 40 GHz with integrated broadband bias-tee, and operational from wavelength 1530 nm to 1620 nm.

- Analysis and simulation of main performance factors of hybrid integrated microwave photonic circuit, including nonlinearities, distortions, and potential degradation sources from optical and electrical domain.

1.4 Thesis Outline

The rest of this thesis is organized as follows: Chapter 2 presents the details of each component and design aspects of the optical receiver, including the analysis of potential degradation factors. Chapter 3 covers the simulation setups and result analyses of the optical receiver developed in Agilent Advanced Design System (ADS). Chapter 4 presents the circuit fabrication details and characterization results of the optical receiver, including comparison with simulation results and justification of the differences. Lastly, Chapter 5 concludes all works accomplished and suggestion for future work.

Chapter 2: Design and Analysis

2.1 Introduction

As an optical-to-electrical converter, the essential components in optical domain are the optical fiber and the photodiode (PD). In terms of implementation, optical coupling loss would be the main issue to reach a high-sensitivity receiver, and it will be further elaborated based on available information.

Switching to the electrical domain, Transimpedance Amplifier (TIA) is the core component that provides first-level signal amplification and current-to-voltage conversion. In the meantime, choosing adequate transmission line type to deliver the signal or to fulfill any specific function shall be evaluated. For instance, a bias-tee circuit is needed on each output trace due to the circuit topology of TIA.

Still in the electrical domain, interconnection method used between components or transmission line is also crucial due to the possibility of signal degradation, especially at high frequencies. Bondwire is widely used to connect circuits but flip-chip method could achieve better performance, and both methods are evaluated. Lastly, some DC bias circuits will be required to assure proper operation of the entire circuit.

In addition to the items mentioned above, another influential factor to the design is the limitation from fabrication equipment, many adjustments would be required in order to be compatible with present equipment and this will be discussed within each corresponding topics.

The next section will start with the components in optical domain, all major aspects of optical fiber and photodetector will be covered in Section 2.2, along with the partial estimation of the optical coupling loss. Next, all electrical components will be introduced in Section 2.3, starting with the TIA, followed by the analysis of interconnection technique applied, selection of transmission line types and the design of ultra-broadband bias-tee. Lastly, Section 2.4 will conclude this chapter.

2.2 Optical Components

2.2.1 Lensed Fiber

Wavelength

In modern gigabit-scale lightwave system, communication operates at wavelength window centered at 1550-nm given that the lowest attenuation of silica fiber lies within this region, and more importantly, it overlaps with the gain spectrum of Erbium Doped Fiber Amplifier (EDFA), an optical amplifier that plays a key role in long-haul communication system.

Coupling Structure

Works presented in [4] [5] have used similar coupling method for the optical signal, which places a lens between the optical fiber and the PD in order to couple the optical signal. This method involves delicate assembly process especially in positioning, which requires precise alignment to collimate the light signal from fiber into the lens, then into the PD. Another variable in this coupling structure is the adhesive used for anchoring the

lens. In addition to accurate optical alignment, aging stability of the adhesive is also an important criterion for successful coupling [7].

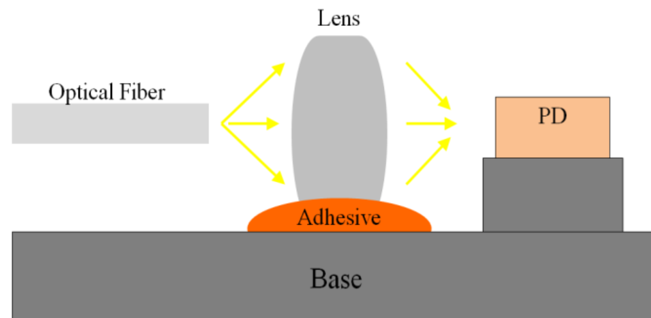

Figure 2.1: Conventional optical coupling structure.

Instead of installing this coupling lens, lensed fiber integrates the focusing mechanism into the fiber itself by shaping its tip, and as a result, it provides a much simpler and efficient solution. Studies in [8] [9] [10] shown that lensed fibers present high coupling efficiency, large misalignment tolerances, and moreover, it is relatively simple to install.

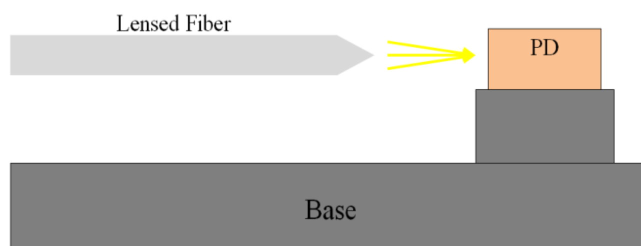

Figure 2.2: Optical coupling structure simplified by using lensed fiber.

Mode-Field Diameter

Given the advantages of lensed fiber, the last item of concern is the Mode-Field Diameter (MFD). Propagation of lightwave is mainly conducted within the core of optical fiber and distributed as a Gaussian function. However, there is still a small amount of light travelling outside of the core, and MFD indicates the diameter at the point where light intensity falls to 13.5% (or $\frac{1}{e^2}$) of its peak value [11], and typically MFD is larger than the core size of fiber. A schematic of light intensity distribution is shown in Figure 2.3.

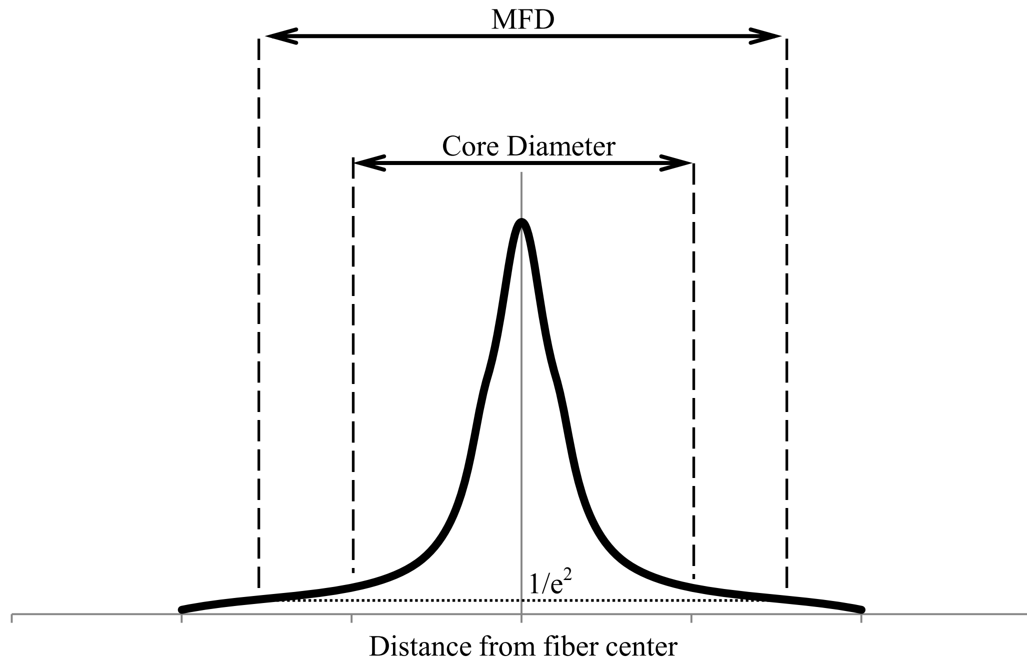

Figure 2.3: Light intensity distribution in optical fiber.

According to the specification, MFD of the PD is 1.5 μm x 2.5 μm. However, the finest lensed fiber achieved from WT&T Inc. is 4.2 μm x 4.5 μm. The coupling loss caused by MFD mismatch can be calculated from [12]:

$$\text{Coupling Loss} = -10\log\left[4\left(\frac{r_1}{r_2}+\frac{r_2}{r_1}\right)^{-2}\right]$$

where r_1 and r_2 are the mode field radii of the coupling ends.

Since both MFDs are elliptically distributed and the rotational angle is unknown, the estimated coupling loss could vary between -1.12 dB to -4.44 dB. Nevertheless, this estimation is only part of the total optical coupling loss, the remaining fraction depends on the alignment accurateness between optical fiber and PD, thus it remains unknown until the fiber is installed and measured, which is presented in Chapter 4.

2.2.2 Photodetector

The main difference of photodetector from regular diodes is the additional intrinsic semiconductor layer between the p-n junction (hereinafter referred to as i-layer), as the Figure 2.4 demonstrates.

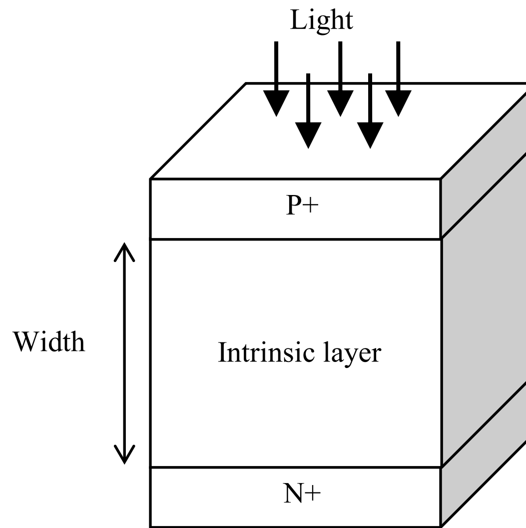

Figure 2.4: Schematic of surface-illuminated photodetector.

Surface-illuminated versus Side-illuminated

Traditional photodetector are surface-illuminated, where incident lights are normal to the surface. Photons will pass through the p-junction then arrive at the i-layer, where the optical-to-electrical conversion takes place. Under reverse biased mode, an electric-field depletion area is formed inside the i-layer, and when incident photons arrive here, new electron-hole pairs are created and thereafter the current flow.

The ratio between photons and electro-hole pairs created is represented by the quantum efficiency, η, and it is dependent to i-layer width. By increasing the width, it

provides greater possibility of catching the photons, but in the meantime, it also increases the traverse time of electrons and holes, resulting slower response and poorer bandwidth.

Side-illuminated PD is an alternative to overcome the drawbacks of surface-illuminated ones, where incident light hits horizontally instead. Under this design, the bandwidth is still controlled by i-layer width, but the quantum efficiency now relies on the depth of i-layer. It has been proven that bandwidth and quantum efficiency are almost independent to each other in side-illuminated PD [13] [14].

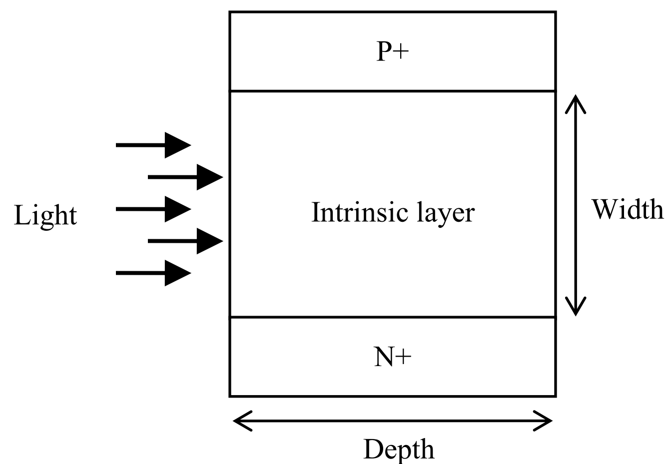

Figure 2.5: Schematic of side-illuminated photodetector.

Responsivity

Quantitative expression of the conversion rate is defined by the responsivity of photodetector, *R*. From the derivation given by [15], responsivity is defined as:

$$R = \eta \frac{\lambda q}{hc}$$

where λ is the wavelength, q is the elementary charge, h is the Planck constant, and c is the speed of light. The unit of responsivity is *Ampere per Watt* (*A/W)*, which indicates the electric current produced for a given amount of optical power, and its value typically falls between 0.6 A/W and 0.8 A/W for broadband side-illuminated PD.

Bandwidth

As previously stated, the traverse time of electrons and holes is a bandwidth-limiting factor. In addition to it, another contributing factor is the RC time constant, composed by parasitic impedance and junction capacitance of PD.

From the perspective of traverse time minimization, thin i-layer seems highly desirable for high-speed operations, but reduction beyond certain extent will also have

by-effects. Once the width is smaller than the Mode-Field Diameter of incident light, the coupling efficiency of light is expected to degrade since partial optical power falls outside of the absorption area [14]. Additionally, the parasitic junction capacitance is inversely proportional to the width of intrinsic layer, thus an over-reduction of the width will end up oppositely to the original intent [16].

PD Selected

In the design of this optical receiver, we have employed a side-illuminated PD from Archcom Technology Inc., model AC6180-C.

There are various PD manufacturers providing PD for 40 Gbps applications, some of them are Picometrix, Enablence Technologies, u^{2}t Photonics, and Yokogawa Electric. However, most of them only offer packaged PD so it cannot be further integrated into other circuits. Archcom Technology and Enablence Technologies both provide die-form PD, but the former has larger bandwidth, smaller junction capacitance and higher responsivity, making it as the best option.

Main PD specifications from both manufacturers are listed in the following table, and the layout of Archcom AC6180 is shown in Figure 2.6, along with the physical dimension.

Parameters	**Archcom AC6180**	**Enablence PDCS12T**
Bandwidth	50 GHz	40 GHz
Responsivity	0.8 A/W @ 1550 nm	0.5 A/W @ 1550 nm
Dark Current	5 nA @ 25°C	2 nA @ 25°C
Junction Capacitance	< 60 fF	< 100 fF
Max. Input Power	6 dBm	N/A

Table 2-1: Main PD specifications from Archcom and Enablence.

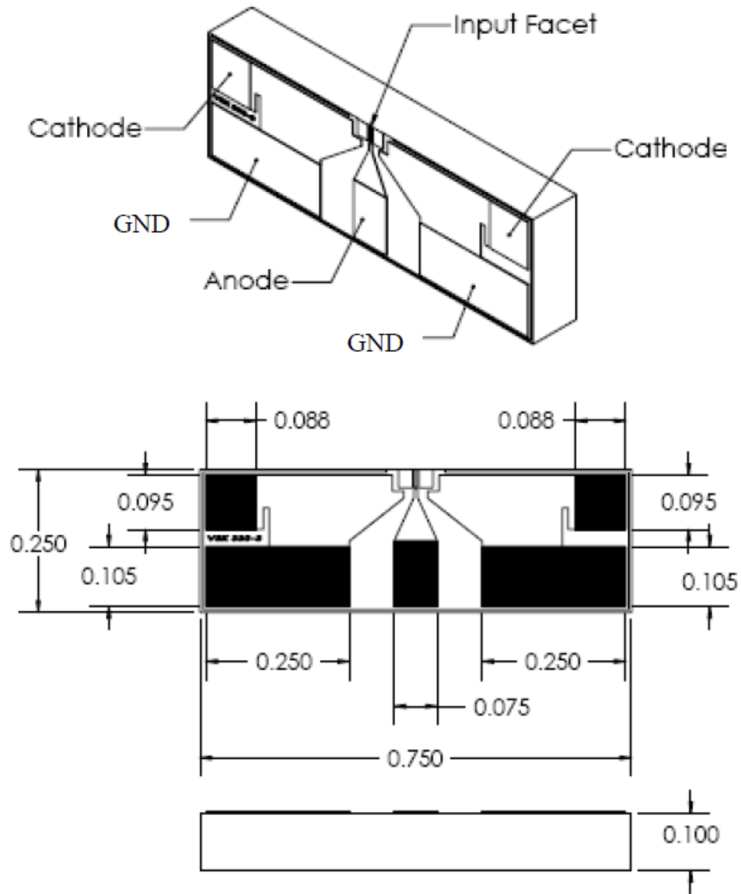

Figure 2.6: Layout and physical dimension of Archcom AC6180, unit in mm [17].

Simulation

Based on the information provided by Archcom, the PD can be modeled as a current source with 60 fF of junction capacitance, marked as C_j in Figure 2.7. It was also provided the equivalent circuit of PD connection pad matched to 50 Ω load, whereas its

schematic is shown in Figure 2.7 and its parameters are C_p = 15 fF, R_p = 0.5 Ω, and L_p = 15 pH.

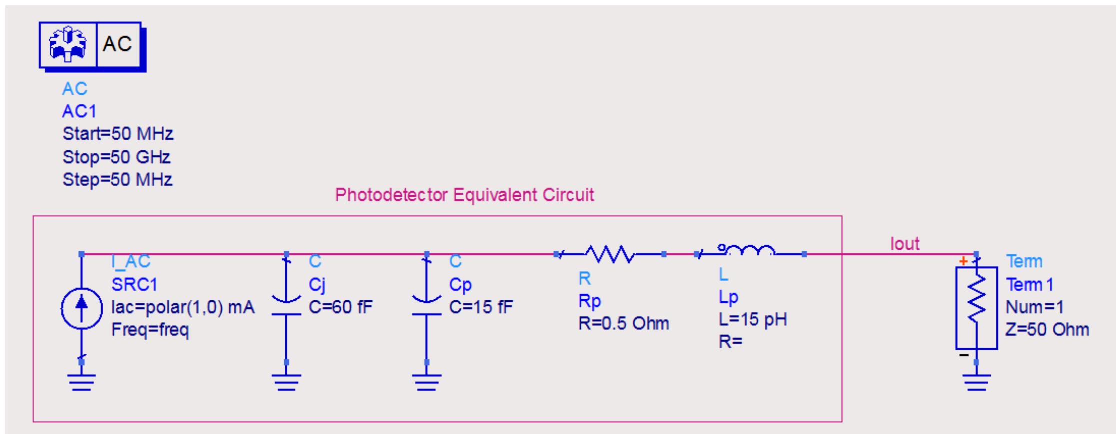

Figure 2.7: Simulation model of PD AC6180 in ADS.

Gathering all information available, a PD model is created in Agilent ADS and its corresponding frequency response is shown in Figure 2.8. The magnitude of output current is not the main item of concern since it changes with the actual input optical power, but it is the 3-dB cut-off frequency that we are interested here, and it is approximately 45 GHz.

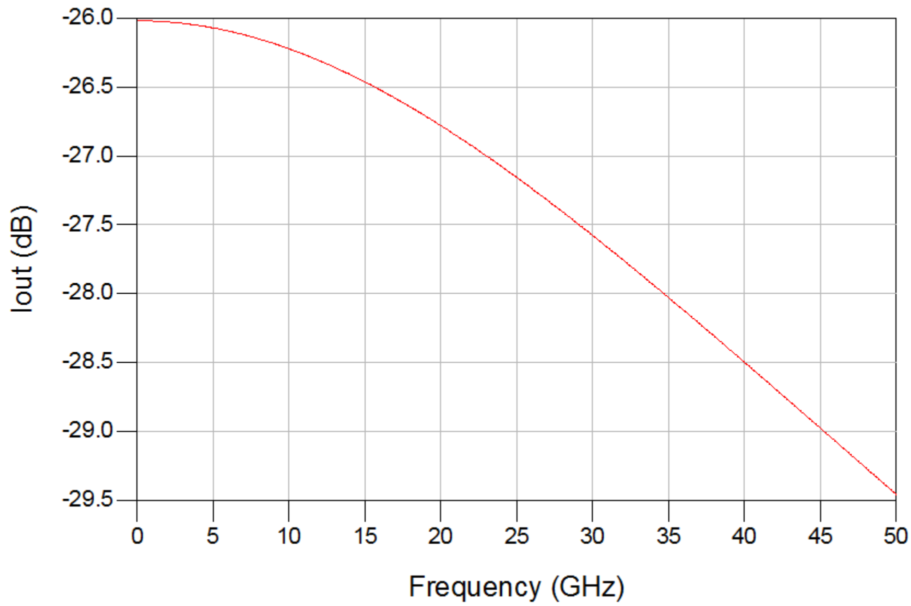

Figure 2.8: Estimated frequency response of PD AC6180.

2.3 Electrical Components

2.3.1 Transimpedance Amplifier

Reason

The output current generated by PD requires a voltage conversion in order to be manipulable by its subsequent circuit. Besides, this raw signal highly needs an amplification process before any distortion or noise adds up. Based on these provisions,

the basic structure of an optical receiver module requires a PD followed by Transimpedance Amplifier (TIA).

Principles of TIA

Shunt-feedback amplifier is the circuit topology prevailing in these years for TIA designs, because it has proven superiority in aspect of bandwidth, transimpedance gain, low noise and other advantages [18] [19]. Figure 2.9 demonstrates a basic shunt-feedback amplifier, where A is the open-loop gain of the operational amplifier (Op Amp for short), C_T is the combined capacitance of PD and TIA, and R_f is the feedback resistance.

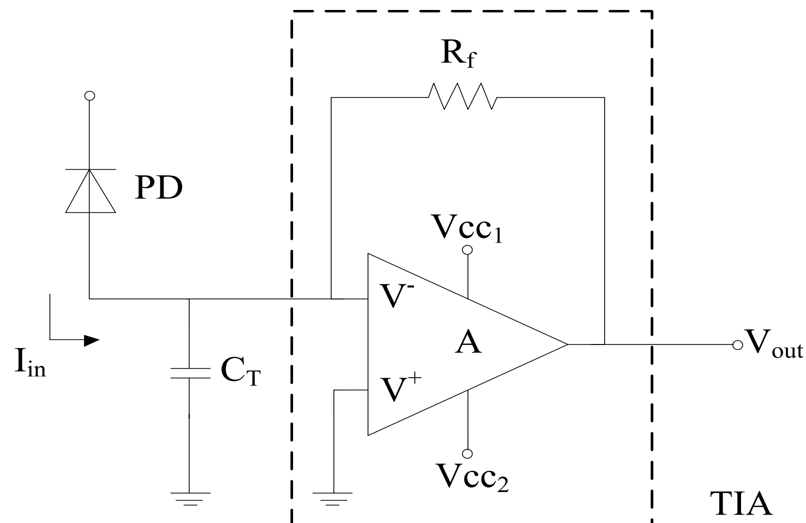

Figure 2.9: Basic schematic of shunt-feedback amplifier

Without other components added, the Op Amp itself will have output voltage as $V_{out} = A(V^{+} - V^{-})$. If $A \gg 1$, it leads to $V^{+} \cong V^{-}$, and since V^{+} is grounded, so does V^{-}, resulting to the so-called "virtual ground" .

The transimpedance value R_T, which can also be interpreted as the gain of the amplifier circuit, is defined as the ratio between output voltage V_{out} and input current I_{in}. By omitting C_T temporarily, their equivalences are $V_{out}=-AV^{-}$ and $I_{in} = \frac{V^{-}-V_{out}}{R_f}$, note that the current flowing into V^{-} port is negligible. After some substitutions, the transimpedance becomes:

$$R_T = R_f \frac{A}{A+1}$$

This result points that the transimpedance value could be independent of the open-loop gain of Op Amp (A) and being simply defined by the feedback resistance R_f if $A \gg 1$. However, the prerequisite here is the formerly stated condition must hold true throughout the operating frequency bands.

The parasitic capacitance C_T is now included in order to verify frequency-dependent factors of the circuit, and the input current becomes $I_{in}(s) = \frac{V^{-}-V_{out}}{R_f} + \frac{V^{-}}{Z_C}$, where Z_C is

the impedance representation of C_T. Substituting the updated equation into the transimpedance formula, it becomes:

$$Z_T(s) = -R_T \frac{1}{1 + s/\omega_p}$$

where $\omega_p = \frac{A+1}{R_f C_T}$. Case ω_p is the dominant pole frequency, and then it will determine the bandwidth of transimpedance amplifier.

Nevertheless, in practical designs, there is another factor to be considered—the bondwire, and its impact could be significant at high frequency bands and related studies are presented in the Section 2.3.2.

TIA Selected

Evaluation of TIA involves several aspects but the main three indicators are bandwidth, transimpedance gain and input-referred specifications, i.e. input overload and input linear range. TIAs from Inphi Corporation, TriQuint Semiconductor, RFMD and GTRAN were investigated and compared, and based on the aspects stated earlier, we have decided to use the solution from Inphi Corporation, TIA 4335TA with 50 GHz of bandwidth, 520 Ω

of transimpedance gain, and 500 μA_{p-p} of input linear range. Electrical specifications of different TIAs are summarized in the following table, whereas better-quality parameters are underlined.

Parameter	**Inphi 4335TA** [20]	**TriQuint TGA4812** [21]	**RFMD SFT-9200B** [22]	**GTRAN GT40-5015TA** [23]
Bandwidth	<u>50 GHz</u>	43 GHz	<u>50 GHz</u>	35 GHz
Transimpedance Gain	520 Ω	235 Ω	<u>1600 Ω</u>	3000 Ω
Input Current	<u>3.0 mA_{p-p}</u>	N/A	2.7 mA_{p-p}	2.5 mA_{p-p}
Input Linear Range	<u>0.5 mA_{p-p}</u>	N/A	N/A	N/A
Output Swing	<u>0.9 V (diff.)</u>	N/A	0.8 V (diff.)	0.7 V (diff.)
Input Equivalent Noise Current Density	35 pA/√Hz	<u>15 pA/√Hz</u>	20 pA/√Hz	<u>15 pA/√Hz</u>
Input-Referred RMS Noise Current	7.5 ~ 10 μA	N/A	N/A	<u>3 μA</u>
Group Delay Variation	<u>± 5 ps</u>	<u>± 5 ps</u>	± 10 ps	± 6 ps

Table 2-2: Electrical specifications of different TIAs.

It is worthy of mentioning the difference of transimpedance gain among the products compared. Circuits from RFMD and GTRAN both have enclosed a post amplifier in addition to TIA, and that explains why their gain is much higher than Inphi's or

TriQuint's. But despite of lower transimpedance gain, TIA from Inphi still has better integrated result.

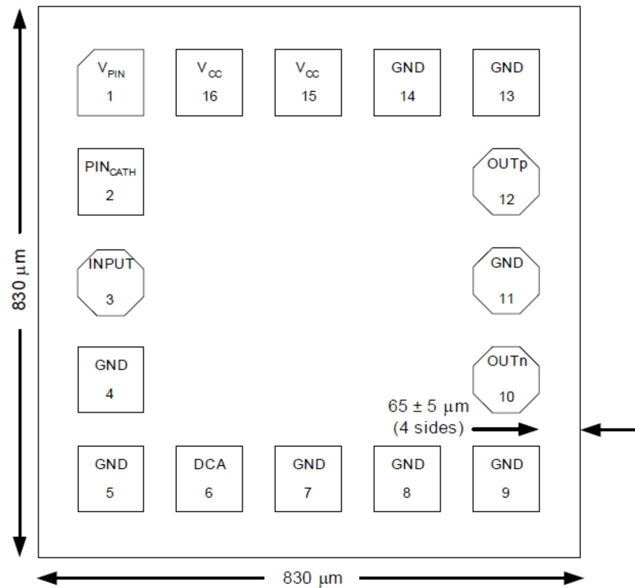

Figure 2.10: Layout of TIA 4335TA [20].

Simulation

S-Parameter file of TIA 4335TA is provided from Inphi for the purpose of frequency-related simulations, yet nonlinearities caused by input overload or output saturation is beyond the extent of the simulation parameters obtained.

In Figure 2.11, the transmission coefficient S_{21} is shown from DC to 50 GHz, varying from 19.6 dB to 12.3 dB, and the output return loss S_{22} ranging from -22 dB to -8.1 dB. These data will serve as a reference for the final circuit of optical receiver, since certain losses or distortions are expected once the circuit is fabricated.

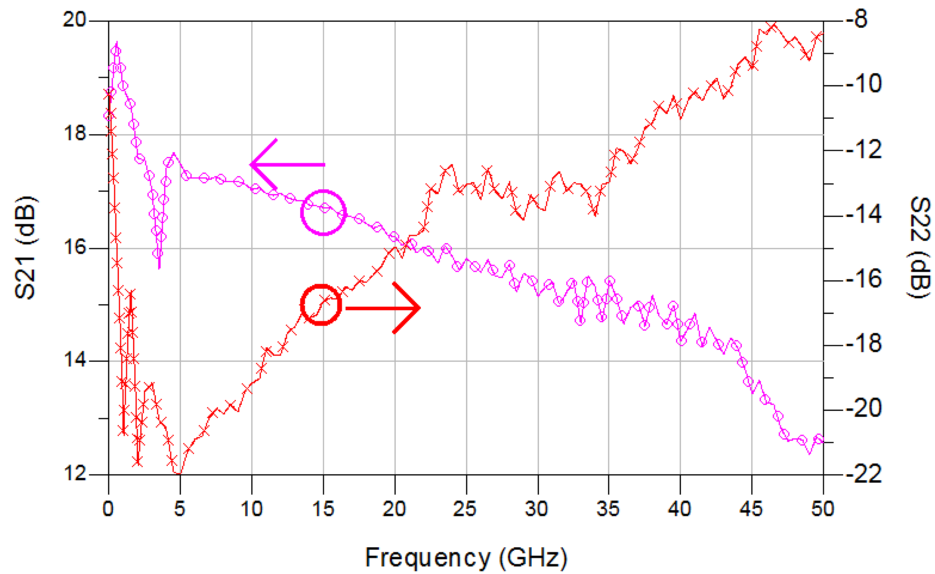

Figure 2.11: S-parameter of TIA 4335TA.

Additional Circuit

According to the manufacturer, circuit topology applied on the output port of TIA is Current Mode Logic (CML), and it requires connection to the voltage source V_{cc} in order

to pull-up the output voltage [24]. Because this voltage pull-up circuitry was not included in the TIA, hence an ultra-broadband bias-tee is required on each output trace in order to block RF signal reaching the V_{cc}, and to remove DC voltage on the connector end, which is in this case, to a 1.85mm RF connector (a.k.a. V-connector). But due to the correlation between bias-tee and transmission line type, details of bias-tee design will be presented in Section 2.3.3 when the output transmission line is brought into focus.

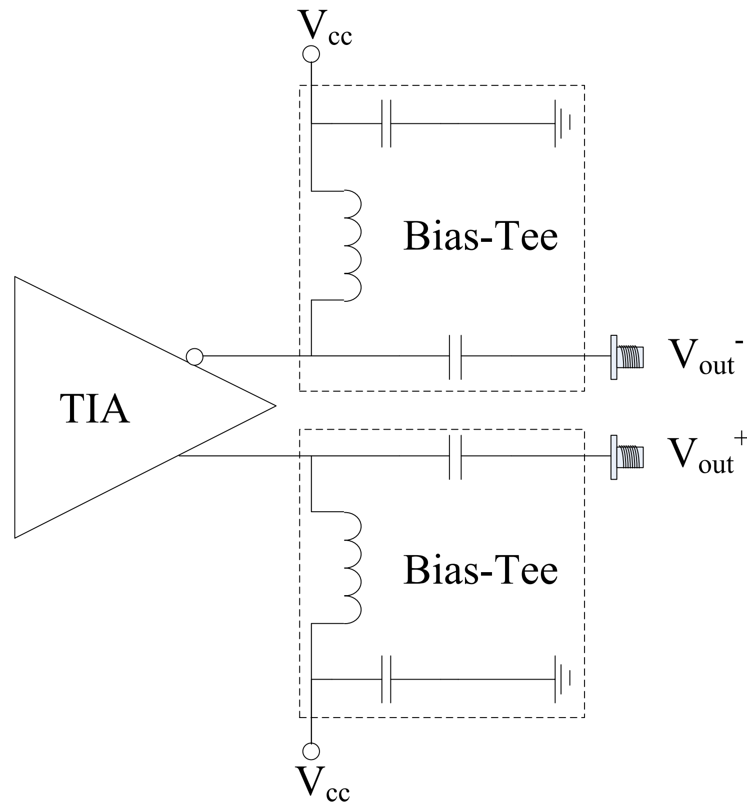

Figure 2.12: Schematic of output transmission line, ended with V-connectors.

2.3.2 Interconnection

Bondwire versus Flip-Chip

The use of bondwire for chips interconnection is widely applied due to its relatively simple technology. Along with the development of millimeter-wave system, numerous studies regarding its electrical characteristics are investigated [25] [26] [27], all because bondwire starts to behave as transmission lines when its physical extent approaches the signal wavelength, and there are several factors that contribute bondwire electrical characteristic, such as shape of bondwire termination and tightness of the wire loop [28], height from ground plane [29], departure and landing angle [30] [31]. But among them all, length is still the dominant factor of high frequency signal decline.

Experiment shows that lengthy bondwire (in this example, 700 μm) could introduce up to 3 dB of insertion loss at 40 GHz [29]. One way to reduce this loss to approximately 0.3 dB is by integrating a five-stage low-pass filter, composed of capacitors and inductors, on both chips [32].

As an alternative to bondwire, flip-chip interconnection technique features with one chip flip over the other, therefore a good transition of signal path is achieved since the

distance is shorter (<50 μm, versus bondwire >100 μm) and introduces less parasitic reactance [29] [33]. Among these reports, only 0.3 dB of insertion loss is observed at 40 GHz in [33], and less than 0.5 dB at frequencies beyond 100 GHz is reported in [29]. This promising result requires high precision equipments for alignment and inspection, in the scale of a few micrometers in order to ensure proper connection, because under this scale, any misalignment could nullify all vantages expected. However, due to the availability of fabrication equipments, and more importantly, the mismatch of pads allocation on TIA and PD, we were unable to apply this interconnection structure.

Simulation

Based on the studies mentioned above, length minimization is still the most efficient way to reduce insertion loss. In this front-end module, there are two signal transitions that will require bondwire: 1) PD to TIA and 2) TIA to output transmission line. Minimum bondwire length estimated for the first transition and the second transition are 127 μm and 135 μm, respectively, and Figure 2.13 indicates the minimum spacing required for each transition of the receiver module.

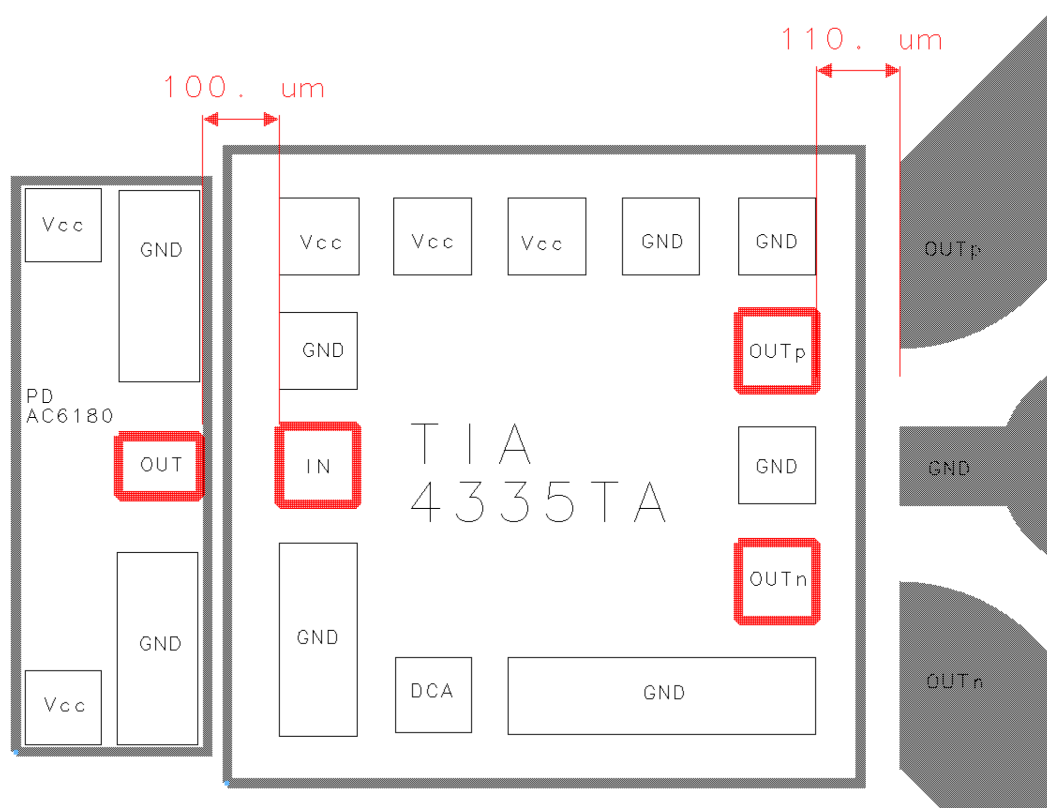

Figure 2.13: Interconnection gaps among PD, TIA, and output transmission line.

Based on the minimum clearance requirements, simulation setups were configured under extreme conditions in order to find the best and the worst case of bondwire effect. The best-case scenario would have the shortest pad distance as well as the lowest height, whereas the worst case goes in opposite configuration, and last of all, all simulations are based on bondwire of 9 μm radius.

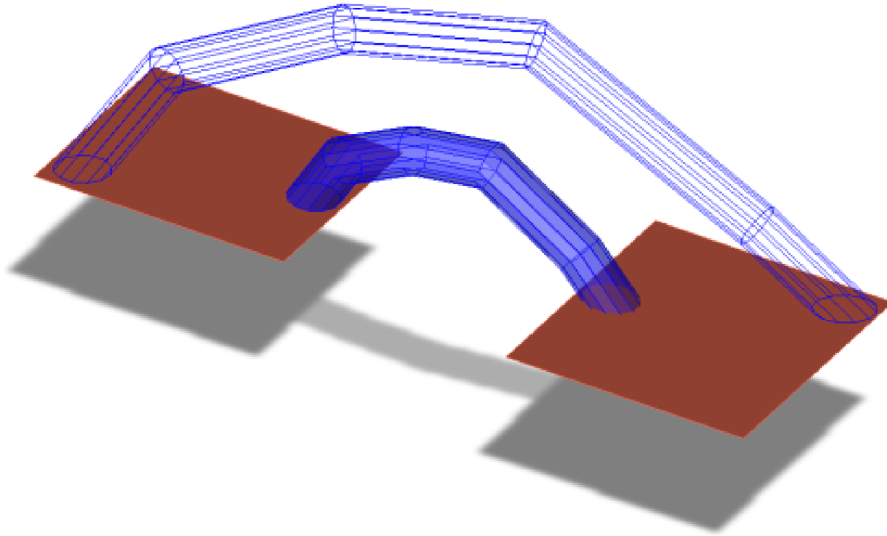

Figure 2.14: 3D model of bondwire simulated; worst case bondwire is connected diagonally.

The wire is segmented into five sections for the purpose of emulating actual bondwire shape, and the simulation is carried out in EMDS, an integrated full-wave 3D electromagnetic solver in Agilent ADS. All lengths and heights measured from the center of bondwire are listed in Table 2-3.

Parameters	1) PD to TIA		2) TIA to Output Trace	
	Best case	Worst case	Best case	Worst case
Length	127 µm	284.5 µm	134.6 µm	377.7 µm
Height	40.6 µm	91.5 µm	43.2 µm	190.5 µm

Table 2-3: Summary of bondwire parameters.

From the simulation result shown in Figure 2.15, the insertion loss caused by bondwire in the first interconnection, PD to TIA, is less than -2 dB in both cases; at 40 GHz, the insertion loss is -1.1 dB for the worst case and -0.6 dB for the best case. In the second interconnection, higher insertion loss is expected because of longer and higher bondwire. The 3 dB cut-off frequency of best and worst case happens at 42.3 GHz and 33.6 GHz, respectively.

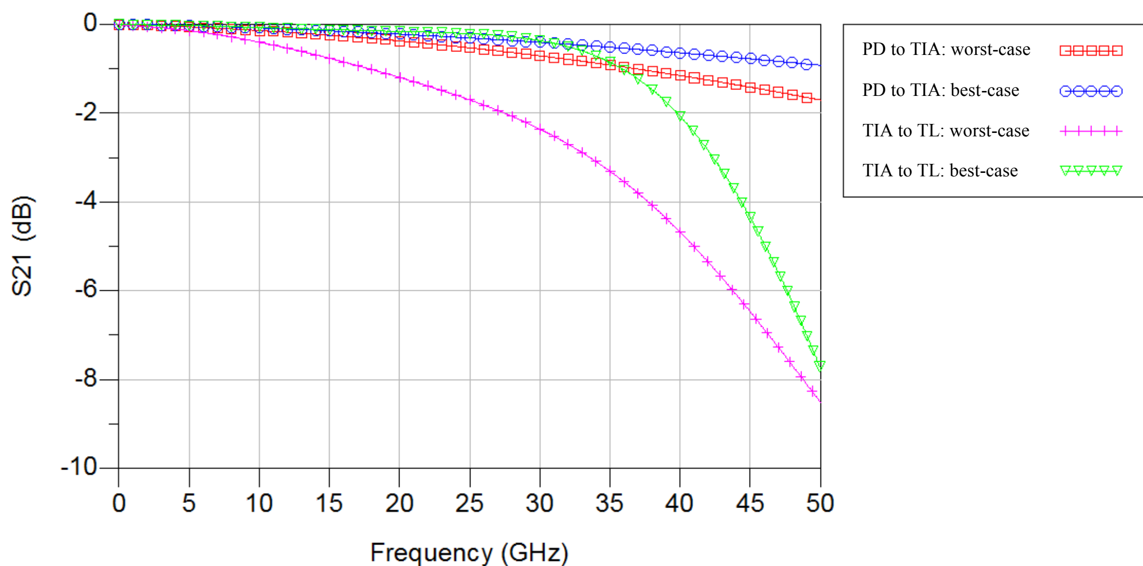

Figure 2.15: Bondwire insertion loss at different length and height.

Despite of the insertion loss, the circuit could be compensated through an amplifier of broader bandwidth. In an ideal amplifier design, bandwidth slightly larger than two-third of the bit rate, $\mathrm{BW} \geq \frac{2}{3}\mathrm{B}$ (BW for bandwidth and B for bit rate), will suffice

the requirement [4] [34]. But actually, the bandwidth is always designed much larger than this ideal value in order to compensate external degradation factors. In this front-end module, the bandwidth of TIA employed varies from 40 GHz to 50 GHz because of the fabrication process variation, and based on the nominal bandwidth-bit rate relation, even with the longest bondwire attached, the module still might reach 43 Gbps ($33.6\ \text{GHz} \geq \frac{2}{3} 43\ \text{Gbps}$), unless, there are other sources of distortion.

2.3.3 Output Transmission Line

Transmission Line Types

When a circuit comes to broadband application, Coplanar Waveguide (CPW) is preferable over microstrip line due to several advantages mainly inherited from its propagation mode, such as lower dispersion, higher resonant frequency, larger characteristic impedance range and lower parasitic capacitances for CPW lumped elements [35] [36] [37].

Also, structural characteristic of CPW (see Figure 2.16) eases the integration of shunt components since there is no need of hole-drilling for ground connection [38], and

from signal's perspective this feature also eliminates parasitic caused by via at high frequencies [39]. On the other hand, CPW structural feature has also become its main drawback, because proper propagation mode demands that both adjacent ground planes must be kept at equal-potential [35], and this is challenging in discontinuities such as junction, bending or lumped elements because of the presence of ground-plane interruption. Consequently, characterization of discontinuities is critical in CPW designs, as well as the elaboration of compensation methods. In summary, handling CPW discontinuities is a more sophisticated issue than microstrip lines [40] [41], because unlike CPW, ground plane of microstrip line is only present at the bottom of the circuit, leaving the design task much simpler. Besides, existing models in CAD tools also accelerate the designing process.

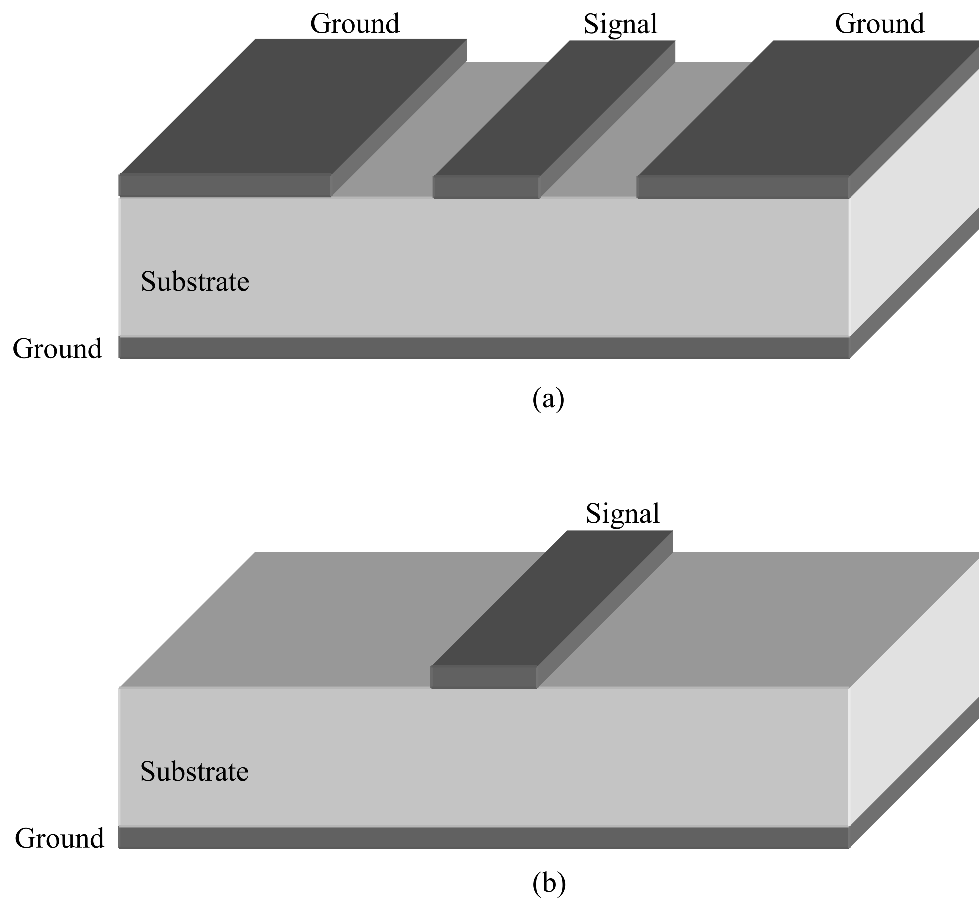

Figure 2.16: (a) Conductor-Backed Coplanar Waveguide (b) Microstrip line.

Design Considerations

Selection criteria of this optical receiver between CPW and microstrip are mainly based on two factors: practicability of implementing ultra-broadband bias-tee and, compatibility with existing fabrication facilities.

The challenge of bias-tee circuit is about the design of lumped components, that is, the capacitor and the inductor shown in Figure 2.12. Since the operational frequency covers from DC to 40 GHz, several parasitic elements are expected at different frequency bands and they must be compensated adequately.

From the fabrication perspective, one of the main limits is the minimum transmission line width achievable, because it influences the frequency response of lumped elements [42] [43] [44]. In collaboration with Centre de Recherche En Électronique Radiofréquence (CREER), the minimum line width provided is 25.4 μm [45], and same for the gap width. Based on these specifications, we have investigated the feasibility of implementing with CPW or microstrip transmission lines, and the details are discussed as follows.

Design Attempts in CPW

Regardless of fabrication technology, there are several transmission line circuits originated from quarter-wavelength concept that are well-developed for bias-tee applications [46], but unfortunately they are not applicable for ultra-broadband circuits,

because the “virtual ground” saw by RF signal is only valid within a small frequency band of the designated center frequency [47] [48], once the frequency surpass this range, RF signal will no longer be “grounded” but spreading through the DC trace. For this reason, the bias-tee will need “real” inductors and capacitors.

Implementation of broadband CPW inductor has already been reported in some studies [49] [50] [51] [52], but their line width and gap width are no larger than 10 μm and 7 μm, respectively, and these values are beyond the fabrication capability of CREER facilities.

Two attempts of CPW inductor are made following the examples shown in [52] and [53], but their corresponding parameters were replaced with the minimum achievable width and gap, and as expected, the results were unsatisfactory because for short wavelength like this, the transmission line shall shrink as well.

Simulation in CPW

The design presented in [52] is simulated as a reference inductor but with two changes. The original GaAs substrate of relative dielectric constant ε_r = 12.9 is replaced by

Alumina with ε_r = 9.9, since this is the substrate used in MHMIC circuit, and, the air bridge used to connect the center of inductor is replaced by a bondwire for simplicity. All geometrical dimensions summarized in Table 2-4.

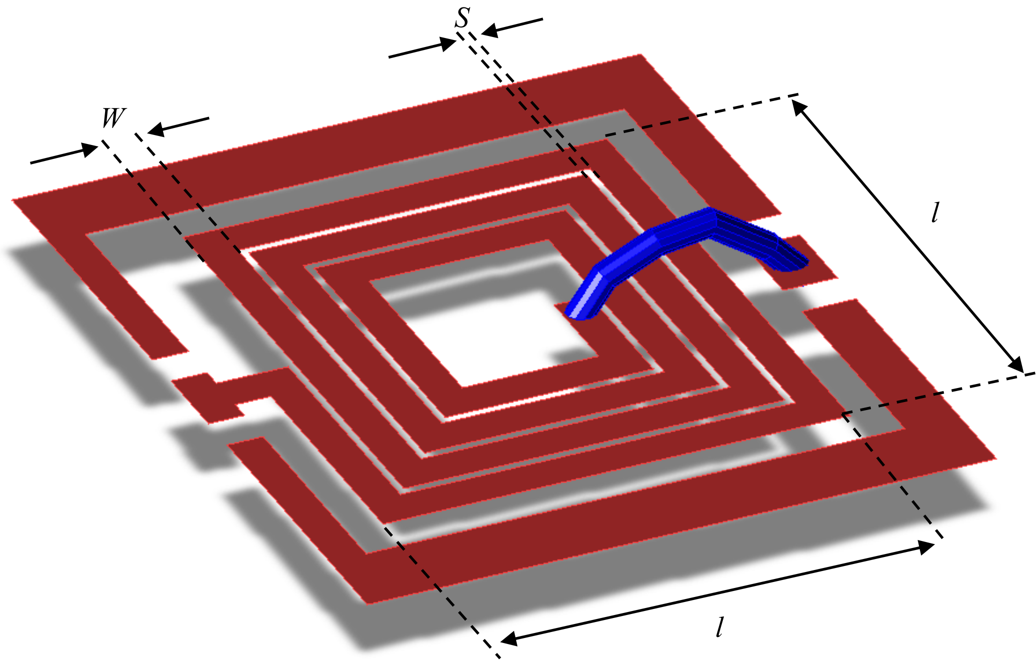

Figure 2.17: CPW inductor.

Parameters	**Reference**	**Design #1**	**Design #2**
Number of segments	15	15	7
Line width, *W*	25 µm	127 µm	127 µm
Gap width, *S*	5 µm	25.4 µm	25.4 µm
Inductor length, *l*	185 µm	1524 µm	1524 µm

Table 2-4: Geometrical dimensions of CPW inductor.

The second design has similar configurations to the first one, but the number of segments is reduced in order to increase the inner diameter of inductor, because larger conductor-free space in the center will improve inductor's Q-factor [54], and this is observed in Figure 2.18: the resonance frequency of Design #1 is slightly shifted in Design #2 from 5 GHz to 8 GHz.

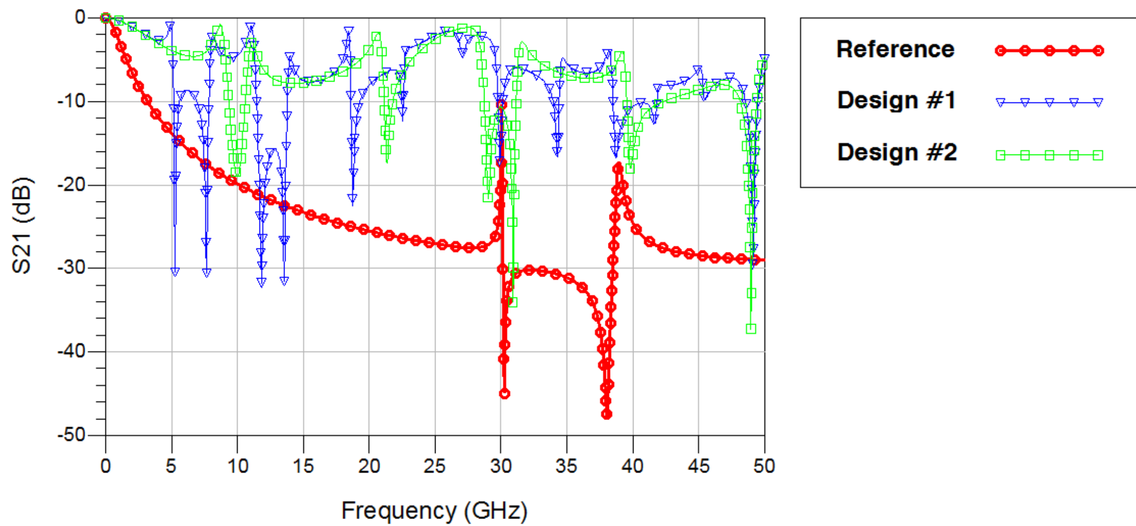

Figure 2.18: S_{21} of CPW inductor in different sizes.

Design Attempts in Microstrip Line

Numerous studies have been carried out regarding microstrip inductor, but once it enters into the domain of millimeter-wave, accurate modelling requires assistance of simulation tools. An equivalent circuit of lumped inductor less than 10 GHz is shown in Figure 2.19 (b), beyond this frequency, because of shorter wavelength, another distributed effects will emerge and some parameters once neutral, such as line width and line gap, will take part of the expanded distributed element model [54] [55], therefore, the final layout must be shaped through several simulation iterations.

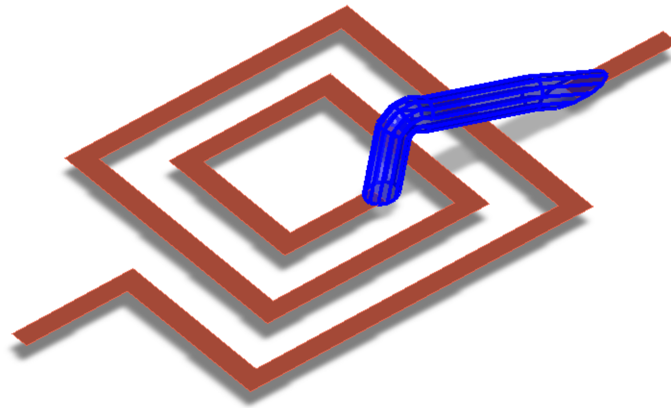

(a)

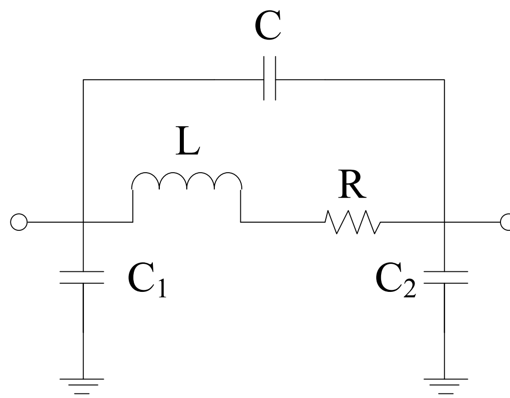

(b)

Figure 2.19: (a) Microstrip spiral inductor with bonding wire

(b) Equivalent circuit of spiral inductor (bondwire effects not included).

Two issues are concluded from the studies of broadband microstrip inductor: poor low-frequency performance and, attachment to advanced fabrication technology. The first issue is expected of microstrip inductor because its maximum inductance value usually is not larger than few nH [56] [57], but the later is a pragmatic issue to continue with

microstrip design because of the compatibility with MHMIC and the availability of the fabrication process such as micro-machining [58] [59] [60].

Simulation in Microstrip Line

Similar to CPW case, microstrip inductor of high resonant frequency is still dependent of the line width. Using the Design Assistant of ADS, a reference inductor is designed without considering fabrication limits, and it is followed by two different inductors that comply with CREER fabrication rules.

Parameters	Reference	Design #1	Design #2
Number of segments	27	27	15
Line width, W	1 µm	25 µm	25 µm
Gap width, S	1 µm	25 µm	25 µm
Inductor length, l	100 µm	2500 µm	2500 µm

Table 2-5: Geometrical dimensions of microstrip inductor.

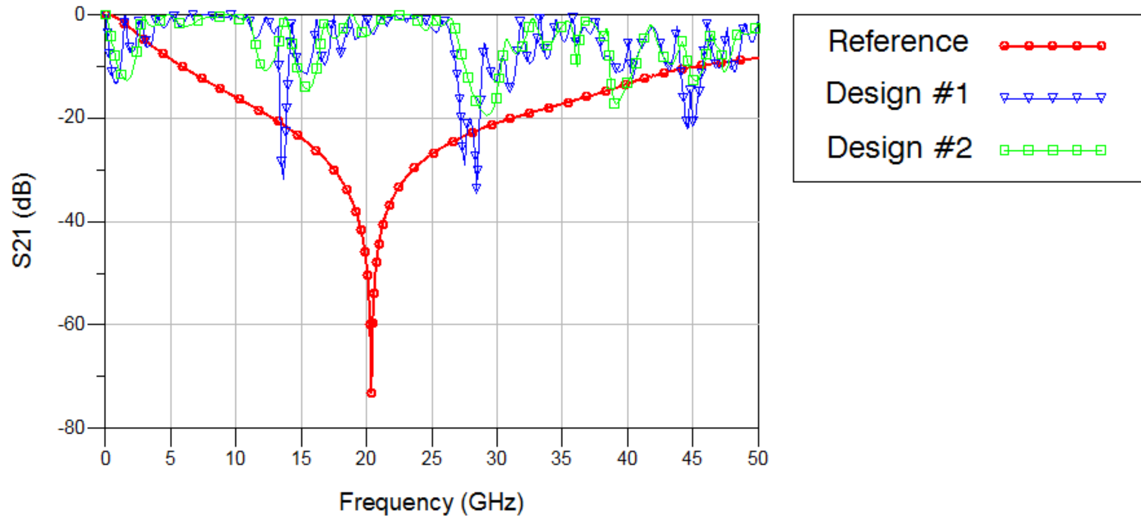

Figure 2.20: S_{21} of microstrip inductor in different sizes.

Final Circuit

Since neither of these transmission lines that comply with CREER fabrication rule can offer satisfactory inductor characteristics, the final solution is to use discrete inductors and capacitors. Broadband conical inductor from Coilcraft, BCR-122 [61], operates from 10 MHz to 40 GHz, and its 1.2 µH inductance will improve significantly the low frequency portion of bias-tee. Standard Surface-Mount Technology (SMT) capacitor from AVX Corporation will serve as DC block and RF filter. GX Series is a 0.1 µF capacitor operational from 16 KHz to 40 GHz, and the insertion loss is less than 0.5 dB

throughout the passband [62]. The main circuit final layout is shown in Figure 2.22 and a core component close view in Figure 2.23.

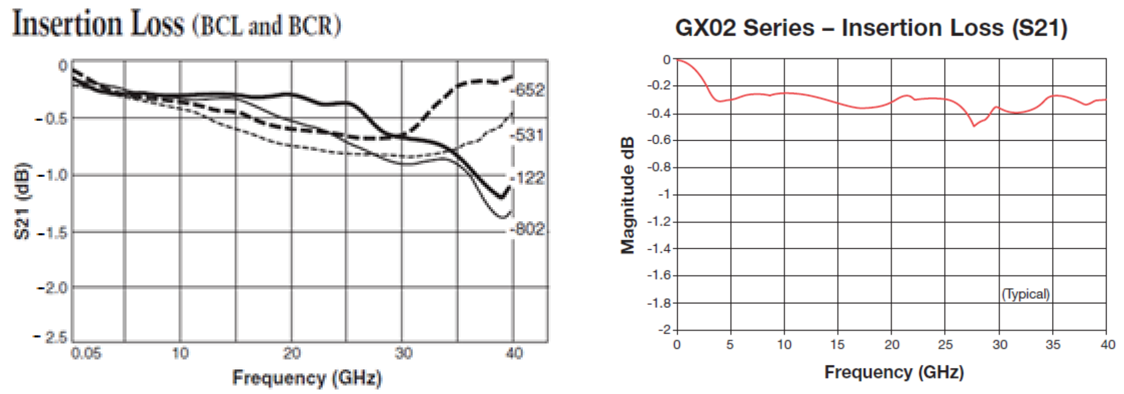

Figure 2.21: Insertion Loss of RF Inductor BCR-122 (left) [61] and RF Capacitor GX02 (right) [62].

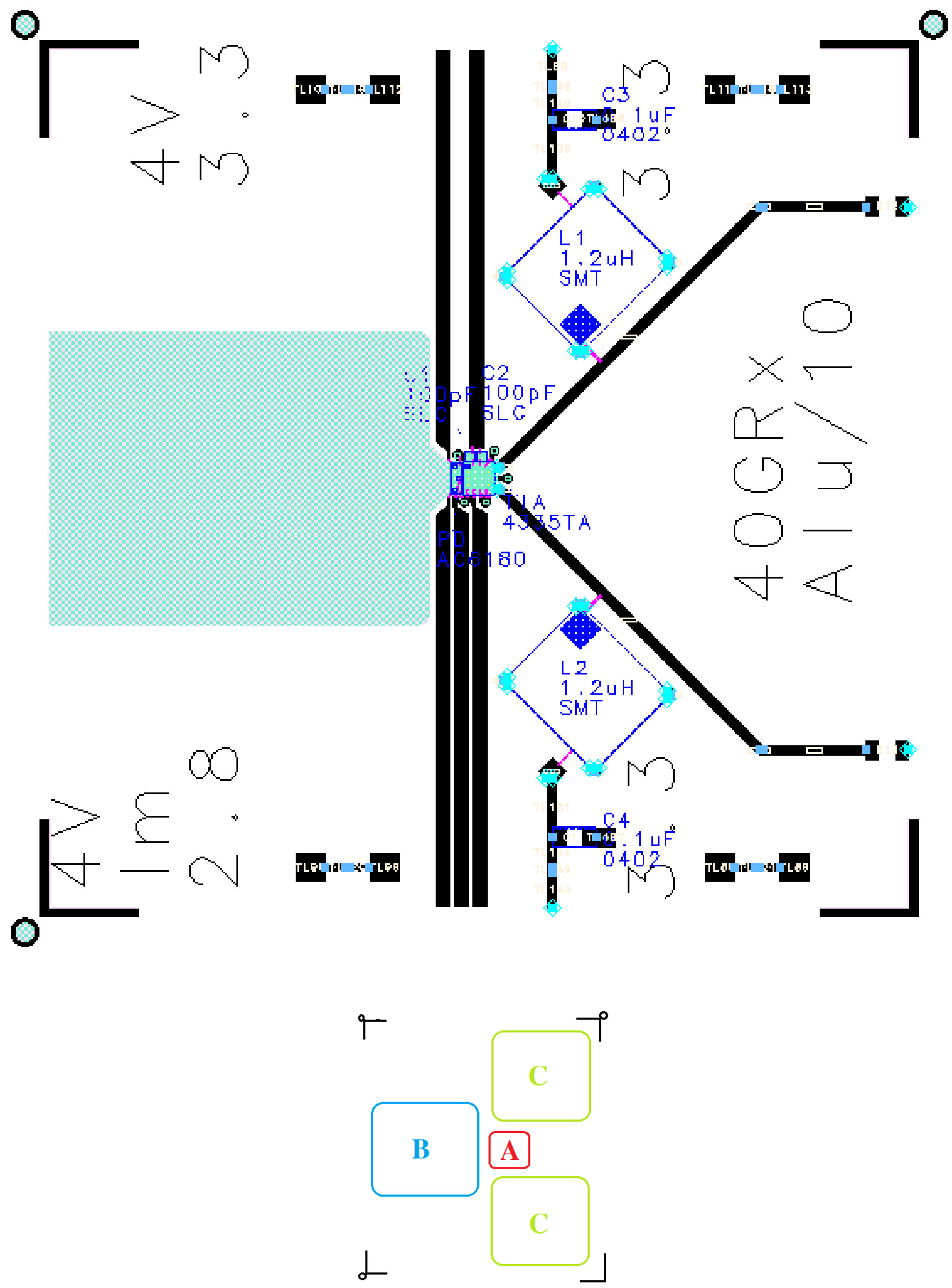

Figure 2.22: Main circuit final layout and area indicators. (A) PD and TIA; (B) clearance reserved for lensed fiber installation; (C) bias-tee.

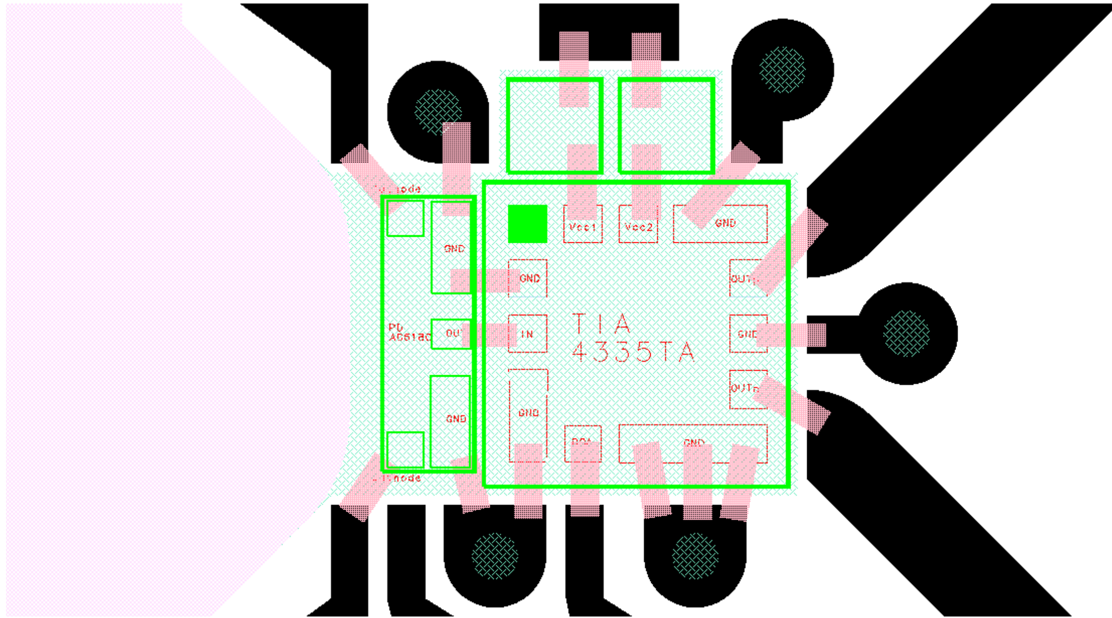

Figure 2.23: Close view of PD (left) and TIA (right) layout. Two single-layer capacitors are placed on top of TIA.

2.3.4 DC Bias Circuit

Supply voltages required for TIA and PD are 3.3 V and 4 V, respectively. To ensure the stability of voltage sources, filters are added on both V_{CC} trace, but an extra microwave capacitor (green squares in Figure 2.23, or C_3 in Figure 2.24 (a)), is placed right before TIA as the last protection measure from any voltage fluctuation. Full component specifications are summarized in Table 2-6.

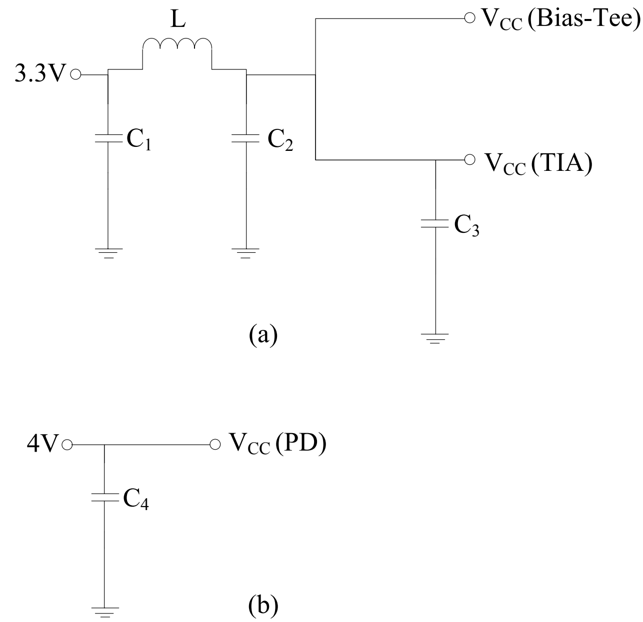

Figure 2.24: DC bias circuit for (a) TIA and (b) PD.

Symbol	**Value**	**Manufacturer**
C_1	4.7 μF	Nichicon, F931D475MBA
C_2	1 μF	AVX, 0402ZD105KAT2A
C_3	100 pF	AVX, GD1030181ZAW
C_4	0.1 μF	AVX, GX02YD104KA72
L	2.2 μH	Murata, LQM21FN2R2N00D

Table 2-6: Component specifications of DC bias circuit.

Layout of DC bias circuit presented in Figure 2.25 contains two sub-circuits and their boundaries are indicated by the L-marker. The upper DC bias circuit will be connected to the top of main circuit (see Figure 2.22), and the lower DC bias circuit to the bottom of main circuit.

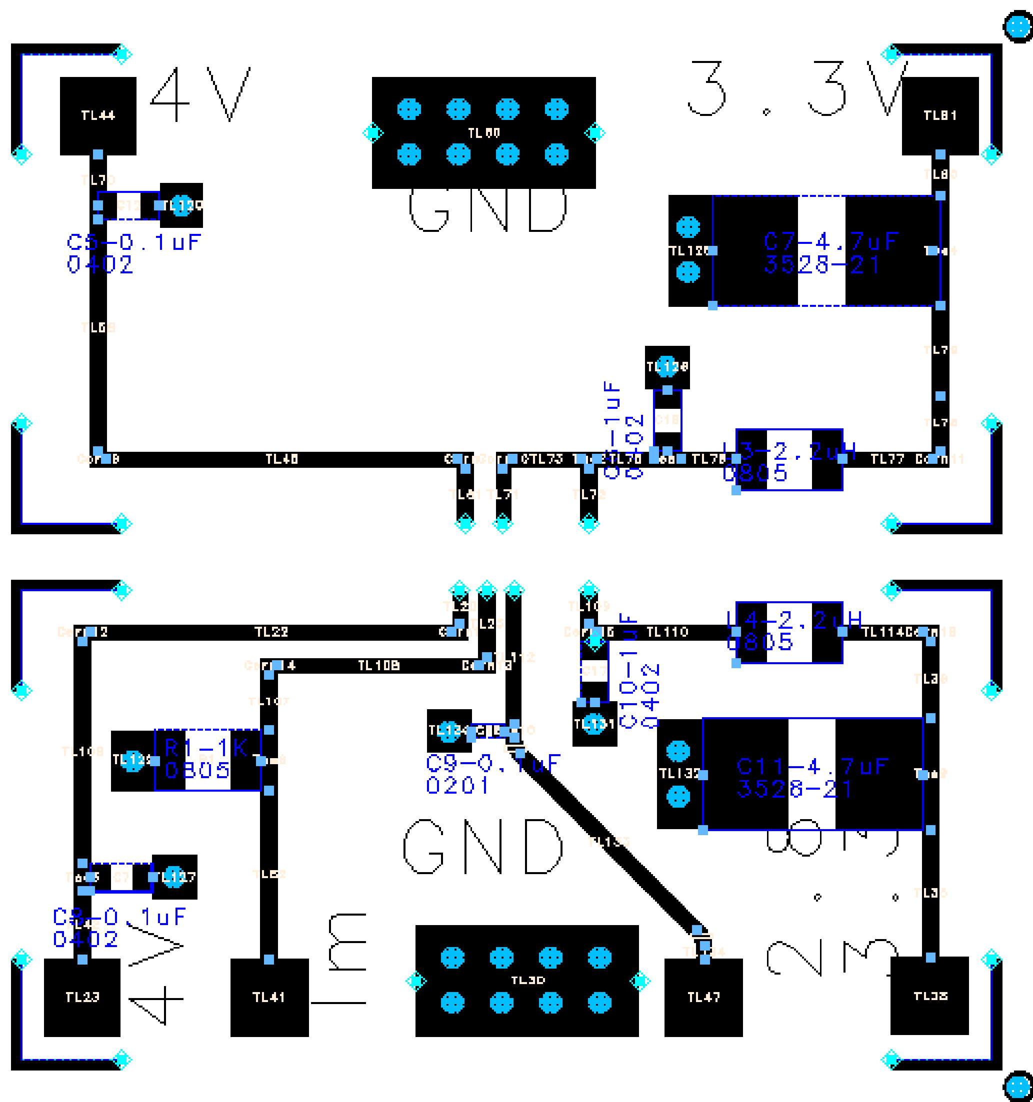

Figure 2.25: Layout of DC bias circuit.

2.4 Summary

In this chapter, we have investigated all main aspects of optical receiver components. Beginning with optical parts, the lensed fiber can provide a simpler coupling structure comparing to regular fiber which requires an extra lens, and side-illuminated PD is suitable for high-speed signal detection because of its structural advantages. Partial optical coupling loss due to MFD mismatch is identified but the total loss can only be known after measurement.

In the electrical parts, the core component TIA is investigated, and the bias-tee is implemented with discrete components because it is unattainable with current facilities for its ultra-broadband characteristic request. For component interconnections, due to the mismatch of pad allocation between PD and TIA, the flip-chip method is not workable thus leaving bondwire as the only option. The dominant factor of high-frequency signal degradation in bondwire is physical length, and its impact are calculated and presented. Lastly, the DC bias circuit with voltage stabilizing design concludes the chapter.

CHAPTER 3: CIRCUIT SIMULATION

3.1 Introduction

Design and simulation of this optical receiver are mainly developed in Advanced Design System (ADS) from Agilent Technologies, and through the co-simulation feature, ADS can provide a combined simulation result from various built-in simulators at different levels of signal analysis, such as ADS Schematic, Momentum, and EMDS. The second simulator is a planar electromagnetic (EM) solver based on Method of Moments and surface (2D) mesh, whereas the later is a full-wave 3D EM solver based on Finite Element Method and volume (3D) mesh. However, the higher mesh refinement in EMDS is achieved through the increase of numerical effort, thus only intricate-volumetric components are simulated in EMDS.

Within the co-simulation setup, S-Parameter and Group Delay of the optical receiver are estimated under the effect of different bondwire length, and their details are discussed in the following section. After that, in Section 3.3, other aspects of interest that could not be simulated are highlighted for further investigation in circuit measurement. To conclude, Section 3.4 summarizes all aspects covered within this chapter.

3.2 S-Parameter and Group Delay

Functional blocks of the optical receiver are identified into four sections: PD, bondwire, TIA and, output transmission line including the bias-tee, as Figure 3.1 demonstrates. Simulations were conducted with best-case and worst-case scenarios based on different bondwire length.

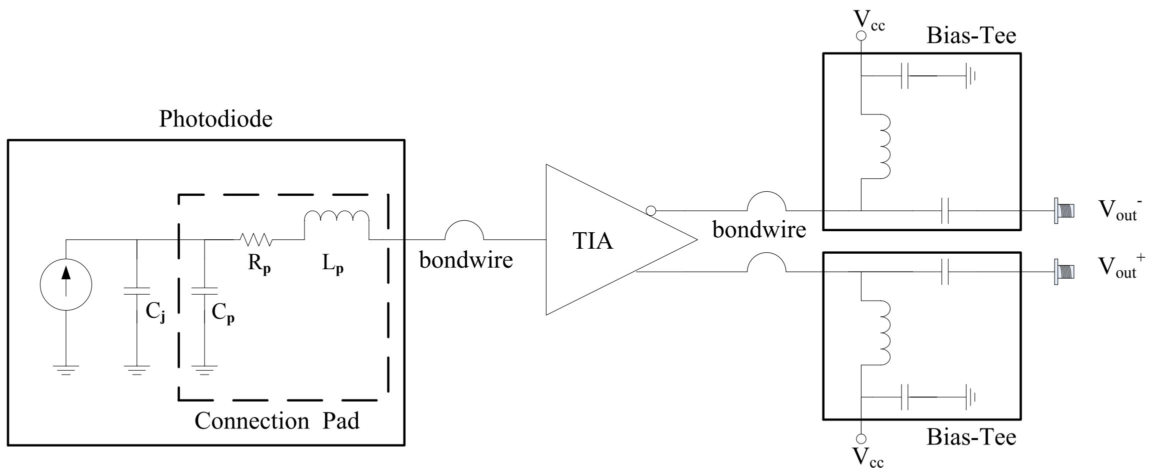

Figure 3.1: Schematic of the optical receiver.

The co-simulation environment incorporates results from three different sources: full circuit transmission lines characterization from Momentum, bondwire characterization from EMDS and, S-parameter files of TIA and RF components of the bias-tee.

S-parameter simulation results are presented in Figure 3.2 and their values are summarized in Table 3-1. Firstly, the transmission coefficient S_{21} of TIA itself is shown with the results of optical receiver as a reference. Also, because the TIA is regarded fully-operational until S_{21} drops to 12.3 dB [20], thus this value is marked as the evaluation baseline and as a result, the estimated bandwidths for best-case and worst-case scenarios are read as 38.9 GHz and 26.7 GHz, respectively.

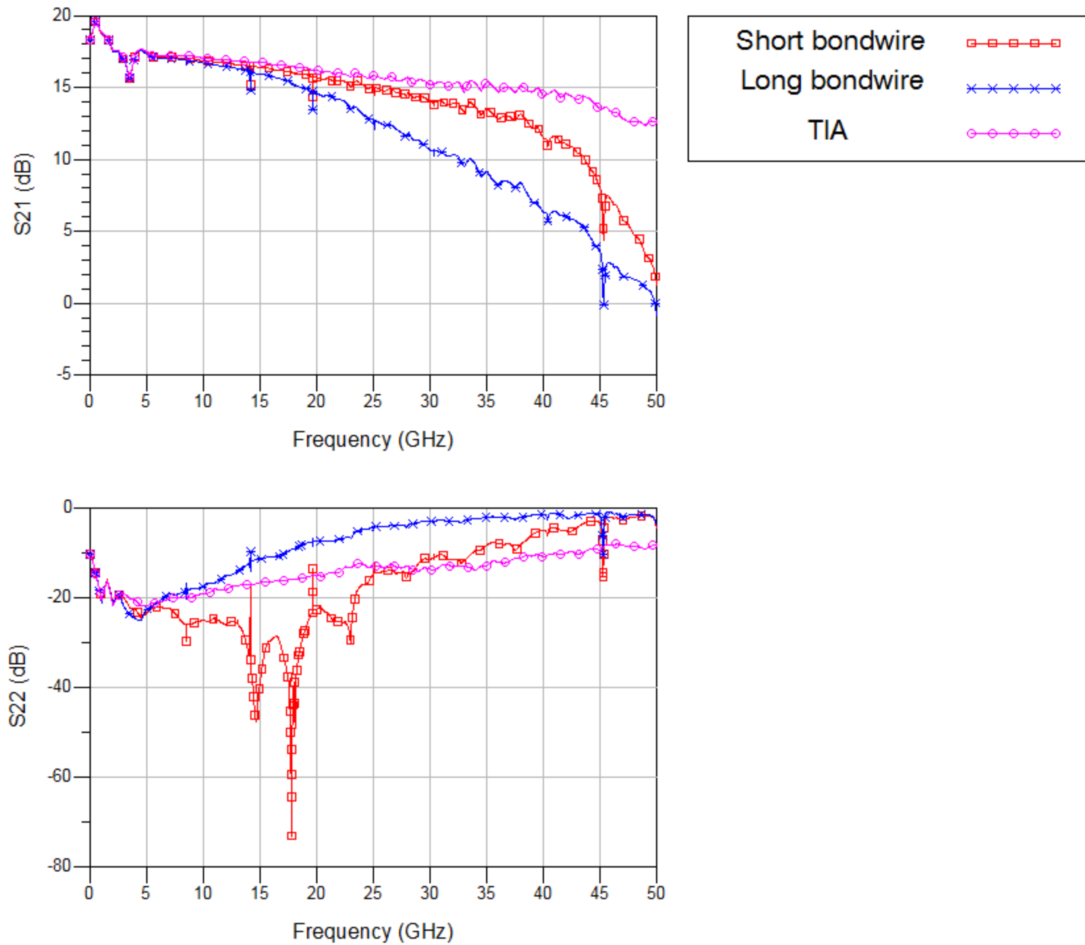

Figure 3.2: S-parameter of the final circuit with different bondwire lengths.

Another parameter of interest is the output return loss S_{22}. Usually it acts inversely to S_{21}, because the degradation of transmission coefficient S_{21} can be interpreted as intensification of losses, which includes the output return loss S_{22}. Preferable value for S_{22} is no greater than -10 dB throughout the operating bandwidth, and according to the simulation result, S_{22} exceeds -10 dB at 33.8 GHz and 17.3 GHz in best-case and worst-case scenarios, respectively.

Scenario	**S_{21} = 12.3 dB**	**S_{22} = -10 dB**	**S_{22} @ 40 GHz**
TIA	—	42.1 GHz	-11 dB
Short bondwire	38.9 GHz	33.8 GHz	-5.1 dB
Long bondwire	26.7 GHz	17.3 GHz	-1.5 dB

Table 3-1: Simulation result of final circuit S-parameter.

Aside from S-parameters, the group delay is also an important parameter that indicates the signal latency at different frequencies. In Figure 3.3, the average group delay for long-bondwire case is read as 160 ps and 145 ps for short-bondwire case, whereas the group delay variation in each case is ±42 ps and ±35 ps, respectively.

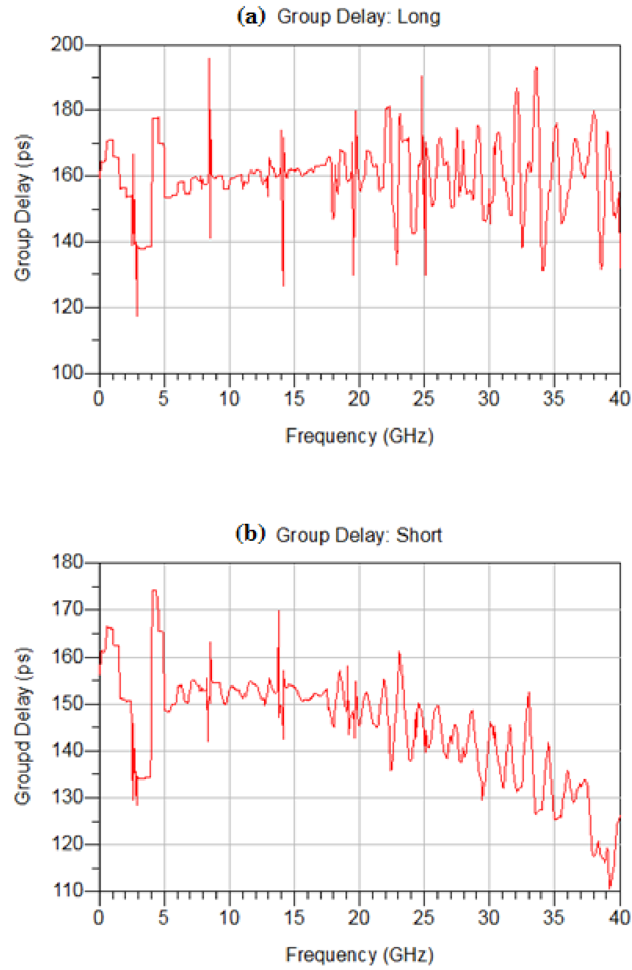

Figure 3.3: Group delay of (a) long bondwire configuration and (b) short bondwire configuration.

3.3 Items bypassed

In addition to items stated above, there are still some aspects of interest that could not be simulated due to insufficient information.

3.3.1 Potential Degradation Factors

The first factor is the impact of bondwire quantity for DC traces. In order to reduce bondwire inductance, the amount of bondwires connecting V_{CC} or ground should always be maximized and kept as short as possible [63]. However, in actual circuit layout, compromise happens because of limited space. Therefore, it is expected to have minor interference on signal integrity, but accurate prediction of distortion magnitude will not be available without a complete circuit information, particularly, the TIA.

Another potential source of signal distortion is the transition from output microstrip transmission line into V-connector. Typical insertion loss of two back-to-back V-connectors varies between 0.3 dB and 0.6 dB from DC to 40 GHz [64]. Moreover, the differences of line width (24 μm for microstrip line and 30 μm for V-connector's pin) and transmission line material will definitely introduce certain losses.

3.3.2 Simulation Analysis

The Harmonic Balance is an analysis method to simulate nonlinear characteristics of the circuit, or more specifically, the amplifier. The simulation aims to identify the signal

strength between the genuine signal and the spurious signals that were created by the amplifier. Nevertheless, the Harmonic Balance simulation has not been carried out because TIA’s nonlinearity information is not contained in the S-parameter file, and no further information would be provided from the manufacturer.

3.4 Summary

Simulation aspects of the optical receiver were covered in this chapter. Based on Agilent ADS, components characterized in different simulator were combined and estimations of S-parameter and group delay were provided. The bandwidth in best-case scenario and worst-case scenario are 38.9 GHz and 26.7 GHz, respectively. However, there were other degradation factors and simulation analysis that could not be proceeded due to lack of information, and their consequences will only be known until actual measurement.

CHAPTER 4: EXPERIMENTAL CHARACTERIZATION

4.1 Introduction

The optical receiver was manufactured in two stages at different institutions. The first phase involves the fabrication and integration of electrical components, and in the second phase the circuit is concluded through the installation of optical fiber.

Evaluation of the optical receiver can be categorized into four groups: optical-to-electrical response, frequency characteristics, nonlinear characteristics and eye-diagram. The first group characterizes the conversion efficiency from optical into electrical; the second group evaluates the frequency performance via S-parameter, group delay and Error Vector Magnitude (EVM); the third group touches the saturation range of the receiver as well as the spurious signals originated from amplifier; lastly, the fourth group analyses the quality of the signal detected.

The following section will start with the details regarding circuit fabrication, including some problems confronted and their work-around. Section 4.3 will present the circuit characterization, covering evaluations of all four groups mentioned previously and

in the exact order. At the end of this chapter, Section 4.4 will wrap up the evaluation done for the optical receiver.

4.2 Circuit Fabrication

Electrical Circuit

The main circuit is fabricated on Superstrate alumina substrate from CoorsTek [65], of 9.9 dielectric constant and 254 μm thick. Two sides of the main circuit are connected to DC bias fabricated on Print Circuit Board (PCB) as Figure 4.1 shows, and they are built on Rogers RO4350B substrate of the same thickness. Underneath the substrates, a 10 mm thick metal base provides support and ground reference for the circuit. The overall circuit dimension ended up to 43.5 mm x 22 mm.

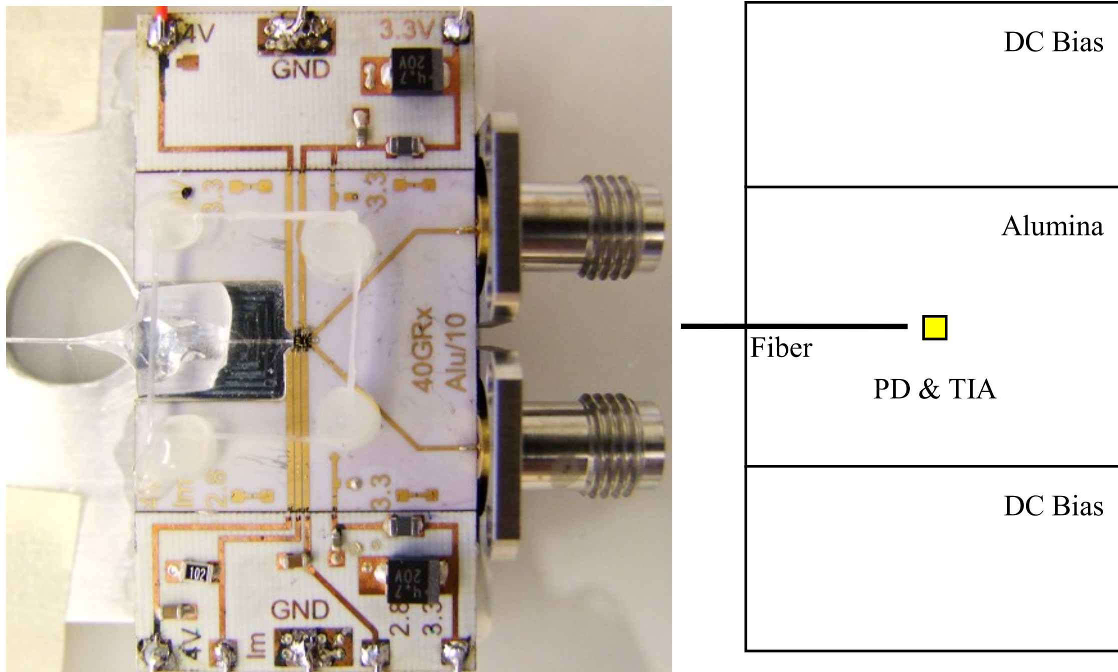

Figure 4.1: Final product of the optical receiver module.

During the fabrication process, two non-recoverable errors were made and their consequences will be explained as follows.

The first issue is about the DC trace filtering. As Figure 2.24 (a) and Figure 4.2 show, a single-layer capacitor C_3 is placed just before V_{CC} enters the TIA, and this single-layer capacitor is directly mounted on the metal base. However, the clearance for installing C_3 was more than expected so it could not be completed. The main concern is the fact that TIA and bias-tee both share the same V_{CC}, even the filtering function of

bias-tee is supposed to block all RF signal reaching V_{CC}, it is still a underlying concern without the last filtering mechanism C_3.

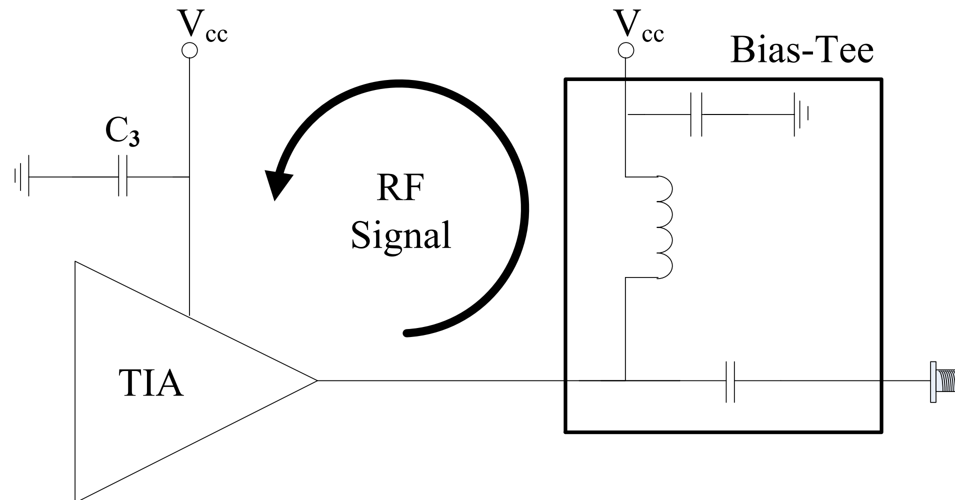

Figure 4.2: Possible RF feedback loop.

After review, we decided to remove the integrated bias-tee and use an external one instead, in order to reassure that pure V_{CC} is fed into the TIA. Bias-Tee module from Picosecond Pulse Labs, Model 5542 [66], is used here. It has 2 dB of insertion loss at 50 GHz and the average group delay is 140 ps.

The second issue is more severe than the previous because it regards the bondwire. It was expected to have seven short bondwires directly connecting the TIA to ground in order to keep low parasitic inductance, but this quantity is reduced to three because

several pads were damaged during wire bonding, and as a result more noise is expected due to this reduction. As stated in the previous chapter, without full information of TIA, it would be difficult to simulate the impact of DC bondwires quantity drop.

Installation of Optical Fiber

The alignment process is extremely sensitive to any vibrations or forces exerted because of the small Mode-Field Diameter of PD. Initially, the fiber is attached to a positioner and moved around PD sensing region until maximum current draw is observed. Once the best position is found, epoxy is added to secure the fiber permanently.

Using a 1550 nm laser source at 4.5 dBm of output power, it is expected to have 0.8 mA to 1.75 mA of current flow, and this variation is because of the rotation angle between lensed fiber MFD and PD MFD. Before applying the epoxy, the maximum current reached was 1.2 mA, but eventually the current dropped to 0.87 mA once the epoxy is added. This result is originated by the liquidity characteristic of epoxy before being totally solidified, if there is any slight difference of the amount of epoxy applied on

either side of the fiber, it will cause to fiber to shift slightly. As a result, the overall optical coupling loss, including MFD mismatch, is -4.13 dB.

Figure 4.3 shows the final position of lensed fiber after the epoxy being solidified. The best working distance of fiber falls between 20 μm to 35 μm, and according to the measurement result depicted in the same picture, the distance between lensed fiber and PD is approximately 25 μm.

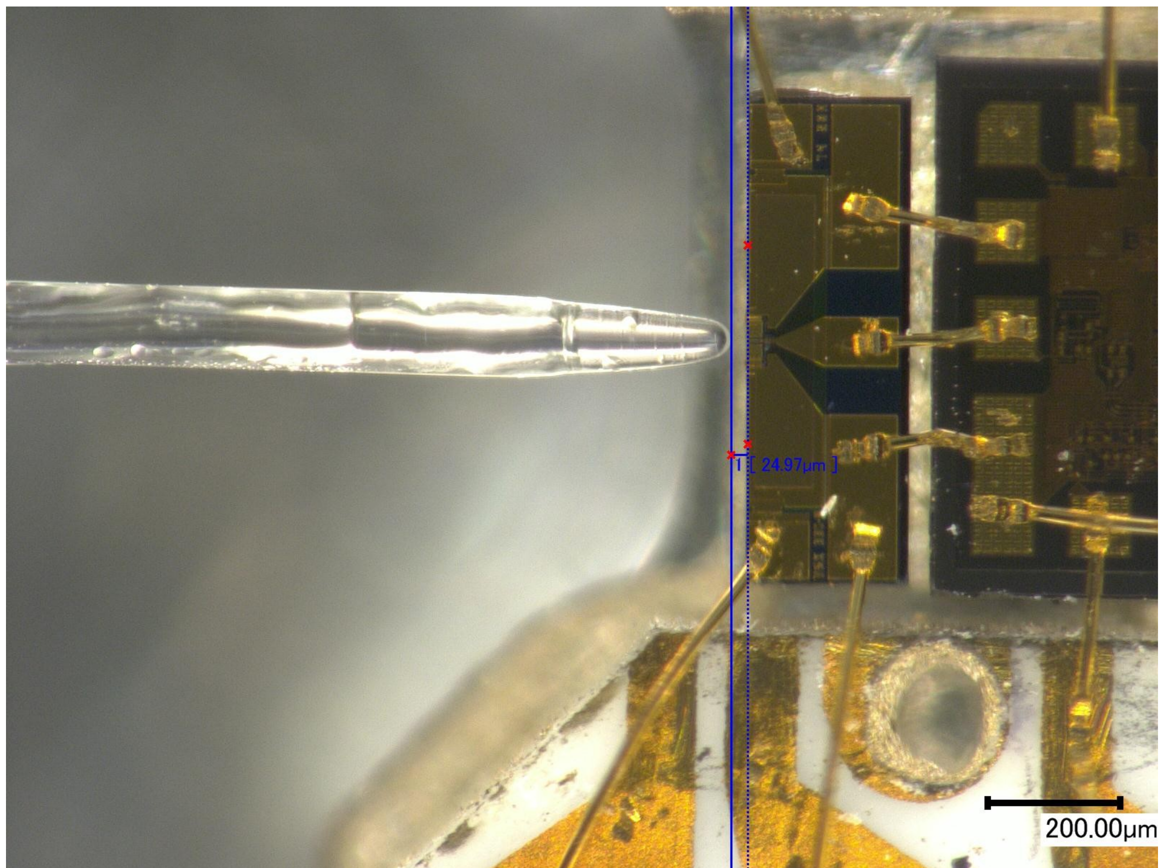

Figure 4.3: Circuit close view after the installation of lensed fiber.

An overview of the circuit core components is shown in Figure 4.4. From left to right are: lensed fiber, PD, and TIA. The rectangular space on top of TIA was originally reserved for single-layer capacitors but they were not installed in the end.

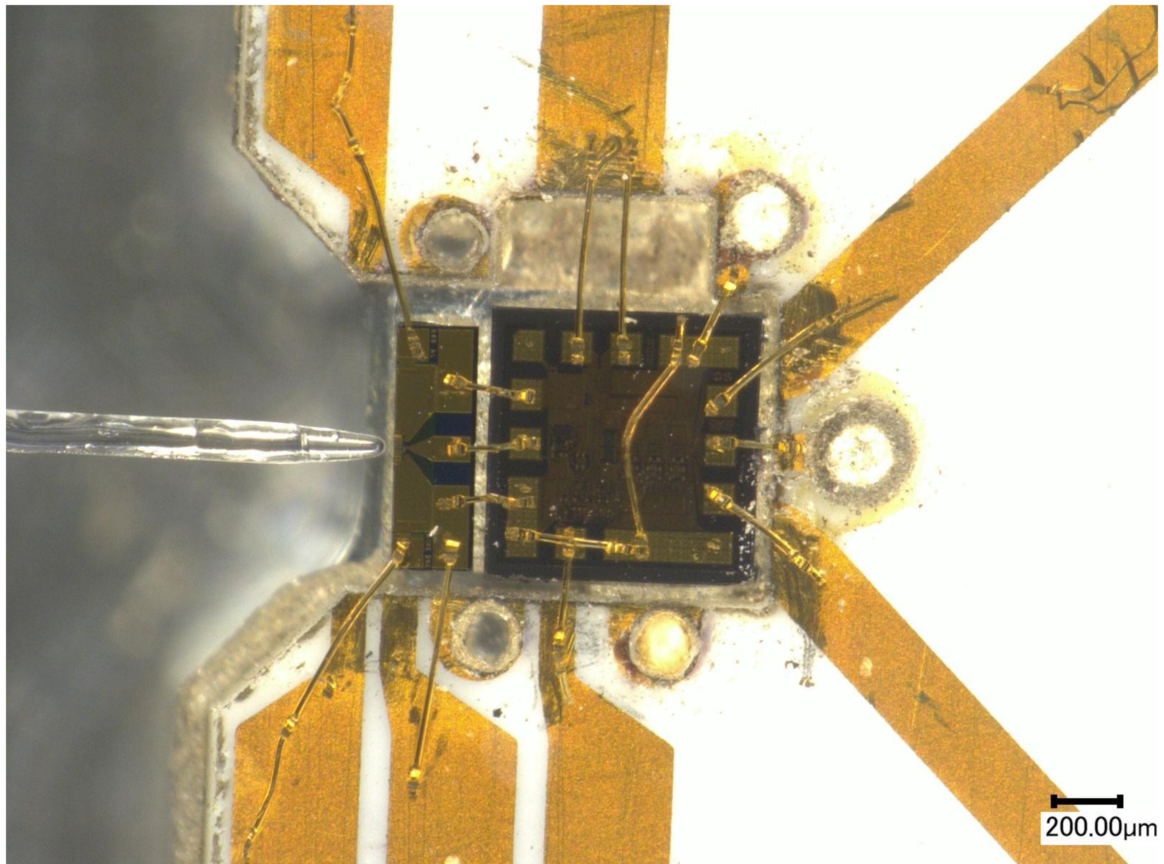

Figure 4.4: Close view of circuit core components.

4.3 Circuit Characterization

4.3.1 Responsivity

Setup

Measurement of the optical-to-electrical conversion rate, that is, the responsivity, is achieved by monitoring the current drew from the power supply of PD and varying the optical input power. In order to boost the maximum optical power for covering wider measurement scope, an optical amplifier (EDFA) and an optical filter is added after the laser source. As a result, the maximum optical input power will reach up to 10 dBm (10 mW), whereas the minimum power starts from -10 dBm (0.1 mW). Measurement setup is shown in Figure 4.5.

Three sets of responsivity were measured, starting from the minimum operational wavelength of PD, 1530 nm, then the most common used wavelength 1550 nm, and lastly the maximum operational wavelength 1620 nm.

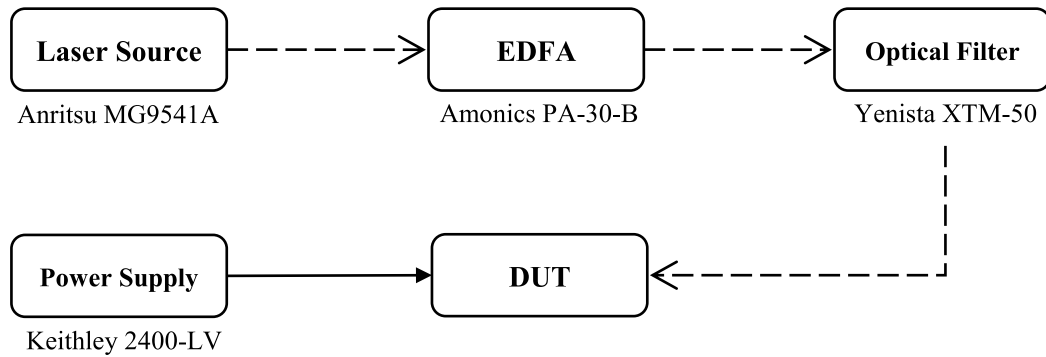

Figure 4.5: Setup for responsivity measurement. Dashed line represents optical link and solid line for electrical link.

Results

Figure 4.6 demonstrates the responsivity of three different wavelengths. The average responsivity at 1550 nm is 0.325 A/W, which translates to -3.91 dB of optical insertion loss since the responsivity of PD itself is 0.8 A/W. Responsivity at 1530 nm and 1620 nm are 0.344 A/W and 0.297 A/W, respectively. Note that at 1620 nm, the maximum optical power of the equipment is limited to 8 dBm (6.31 mW).

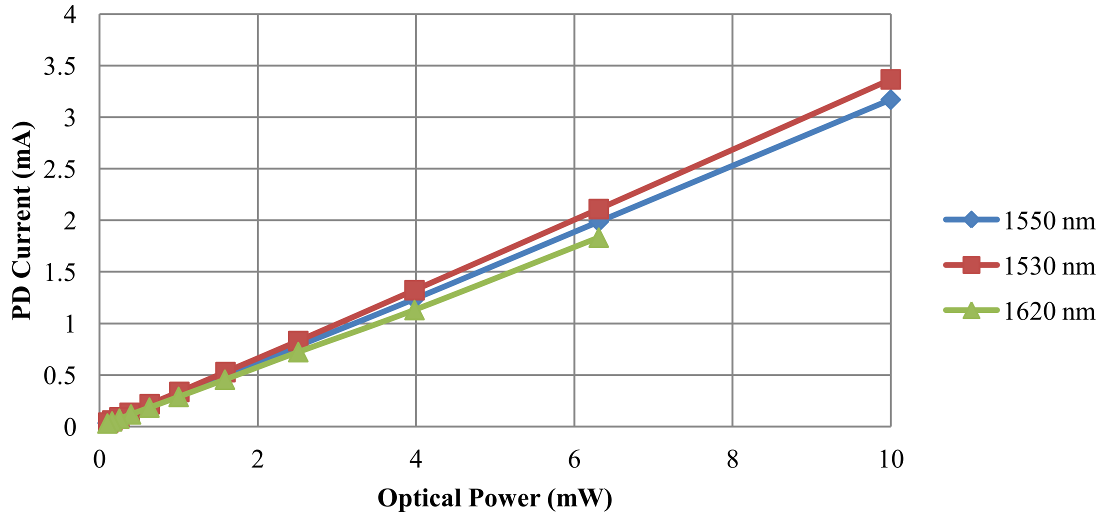

Figure 4.6: Responsivity of optical receiver.

4.3.2 S-Parameter and Group Delay

Setup

First step of the measurement is to collect a reference data because the Mach-Zehnder Modulator (MZM) itself presents both optical and electrical losses. This reference data is completed by placing a 100 GHz photodetector from u^2t Photonics AG [67] as the DUT shown in Figure 4.7. Since the electrical insertion loss of 100 GHz PD is almost zero from DC to 40 GHz, therefore this reference data will mainly contain electrical

characteristics of the MZM only, and we can remove MZM effect once the DUT is replaced with our optical receiver.

During the measurement, a laser source of 1550 nm wavelength from Alcatel [68] was set to 13 dBm and connected to Oclaro MZM [69], which has 4.5 dB of optical loss at 1550 nm and 5 dB of electrical loss at 40 GHz.

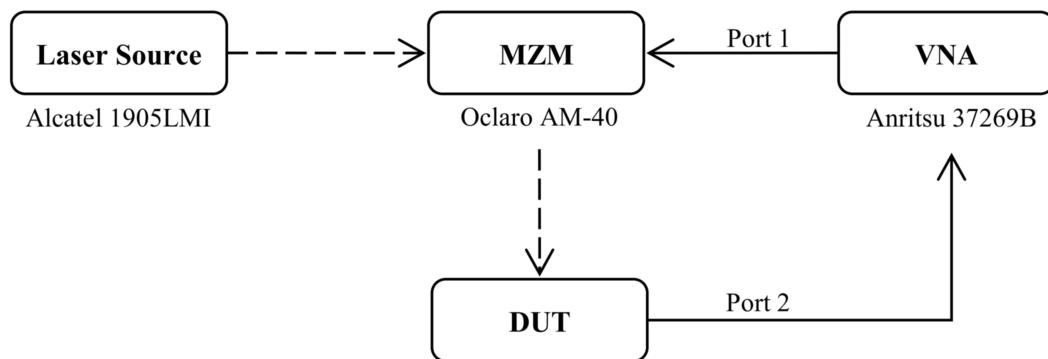

Figure 4.7: Setup for S-parameter measurement.

Results

Original measurement results without compensation are depicted in Figure 4.8. Aside from the ripples shown between 20 GHz and 30 GHz, after 30 GHz the S_{21} has declined

approximately 12.5 dB from its maximum value, and beyond this point the signal may no longer be recognizable.

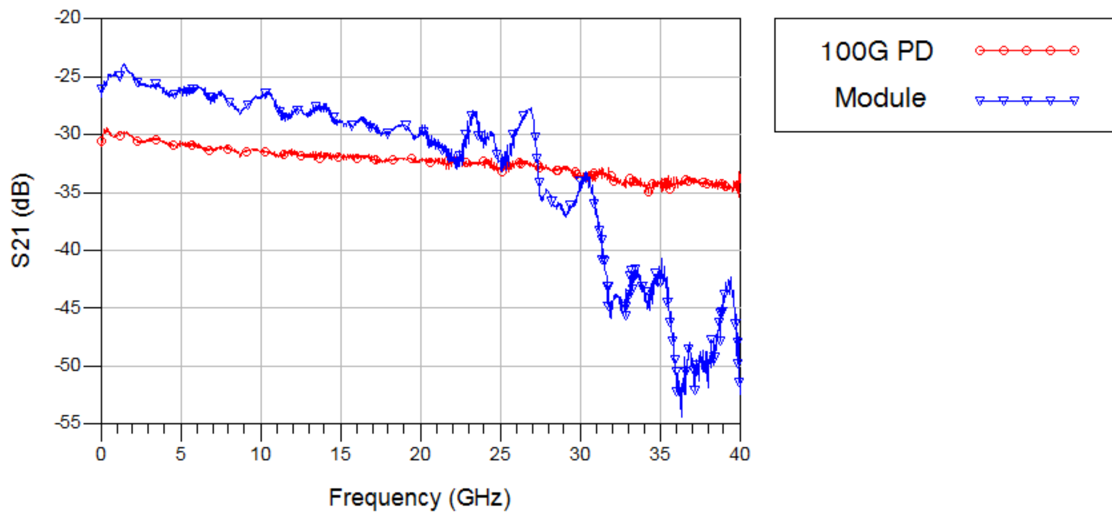

Figure 4.8: S_{21} response of the reference circuit and the optical receiver module.

Fluctuation between 20 GHz and 30 GHz are identified once the bias-tee had been characterized. As Figure 4.9 shows, within that frequency band the ripples of bias-tee itself can reach up to 3 dB.

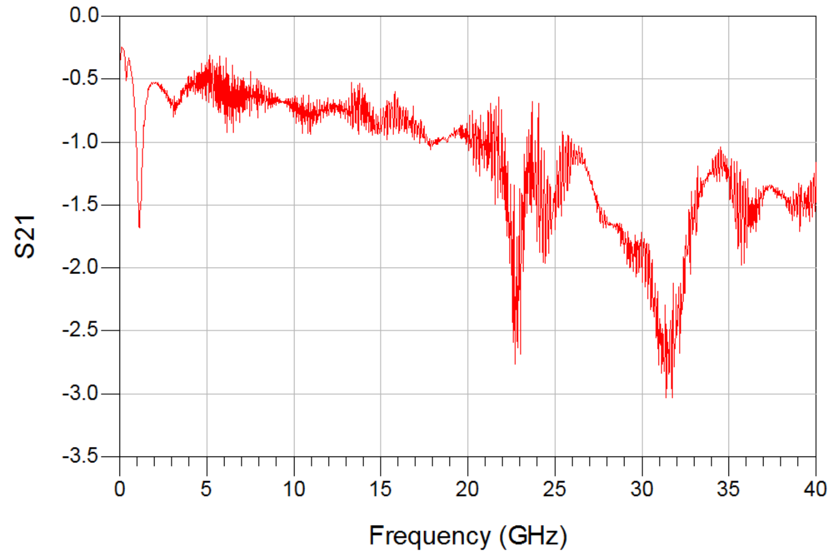

Figure 4.9: S_{21} response of the bias-tee from Picosecond Pulse Labs.

The sharp drop after 30 GHz is likely to be caused by reaching the resonant frequency of the module. A measurement report from TIA's manufacturer shows, with ten 180-μm long bonding wires connected to ground, the total parasitic capacitance to ground from top metal layer is approximately 0.4 pF, and the total parallel equivalent inductance of all bonding wires to ground is approximately 15 pH. These values will give the resonant frequency to 65 GHz. However, the actual circuit has less than ten bonding wires and the lengths are much longer, resulting lower resonant frequency.

To remove the effects of MZM and bias-tee on our optical receiver, their S_{21} are subtracted from the S_{21} of our optical receiver, and the resulting response is shown in Figure 4.10.

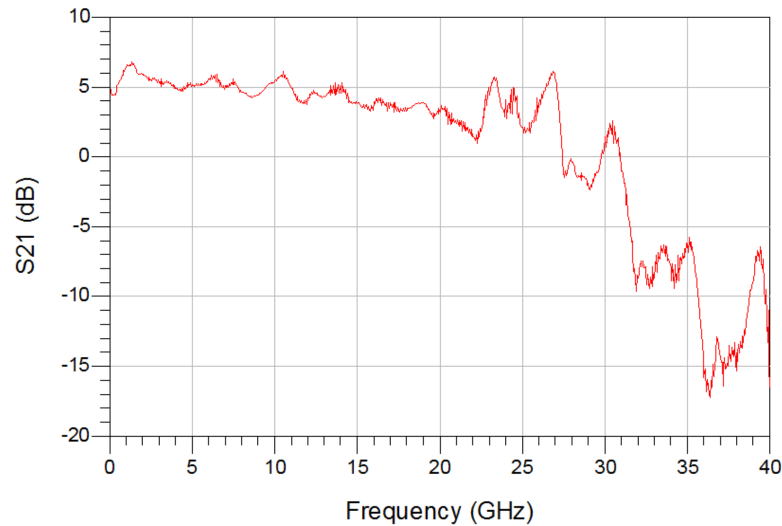

Figure 4.10: Compensated S_{21} of the optical receiver.

Still from the S-parameter measurement, it also contains information regarding the group delay. In Figure 4.11, the average group delay measured is 17.7658 ns, and this increment, comparing to the simulation result, is partly due to the series adapter added in between the module and bias-tee, of approximately 7 cm long, plus the group delay of bias-tee itself. Nevertheless, the group delay variation is confined to ±68.5 ps.

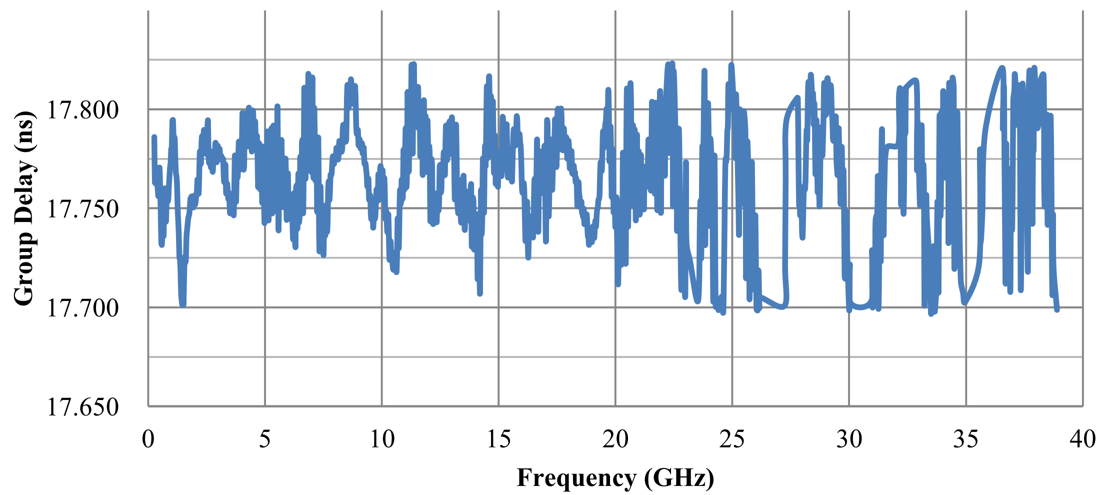

Figure 4.11: Group delay of the optical receiver.

4.3.3 Error Vector Magnitude

By indicating the deviation of constellation points between ideal positions and received signals, the Error Vector Magnitude (EVM) serves as an evaluation measure for the transmitter or receiver in a communication system.

In order to carry out the assessment, standard WiMedia Ultra-Wideband (UWB) signal is generated and uploaded to the optical link. The signal is later converted back into electrical form by our optical receiver, then demodulated and verified by a signal analyzer.

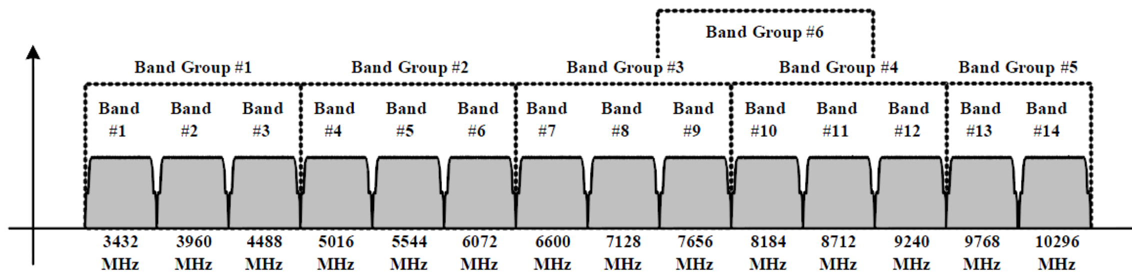

Figure 4.12: Spectrum of UWB [70].

From the UWB spectrum allocation, as Figure 4.12 shows, the maximum signal band is only at 10.296 GHz, therefore to validate the optical receiver in MMW scale, both signal up-conversion and down-conversion are required before and after the optical transmission.

Setup

In the evaluation environment, up-conversion of UWB signal is achieved optically. Based on the nonlinear response of MZM, its second harmonic generation will double the frequency of the signal applied. As shown in Figure 4.13, a Local Oscillator (LO) at 13.175 GHz is applied on a high speed Dual-Electrodes MZM from SOCBN, and using an 180° hybrid coupler, ideally, only even-order sidebands will be generated. Due to the

high electrical insertion loss of MZM and hybrid coupler, a RF amplifier is added to counteract the losses.

Later, the second DE-MZM from Fujitsu will modulate the UWB signal from an Arbitrary Waveform Generator (AWG) into the optical link. UWB of Band Group #1 centered at 3.96 GHz is used for the measurement, and the data rate is set to 480 Mbps. Lastly, to identify the effect of RF input power, a Variable Attenuator is inserted for power sweep purpose.

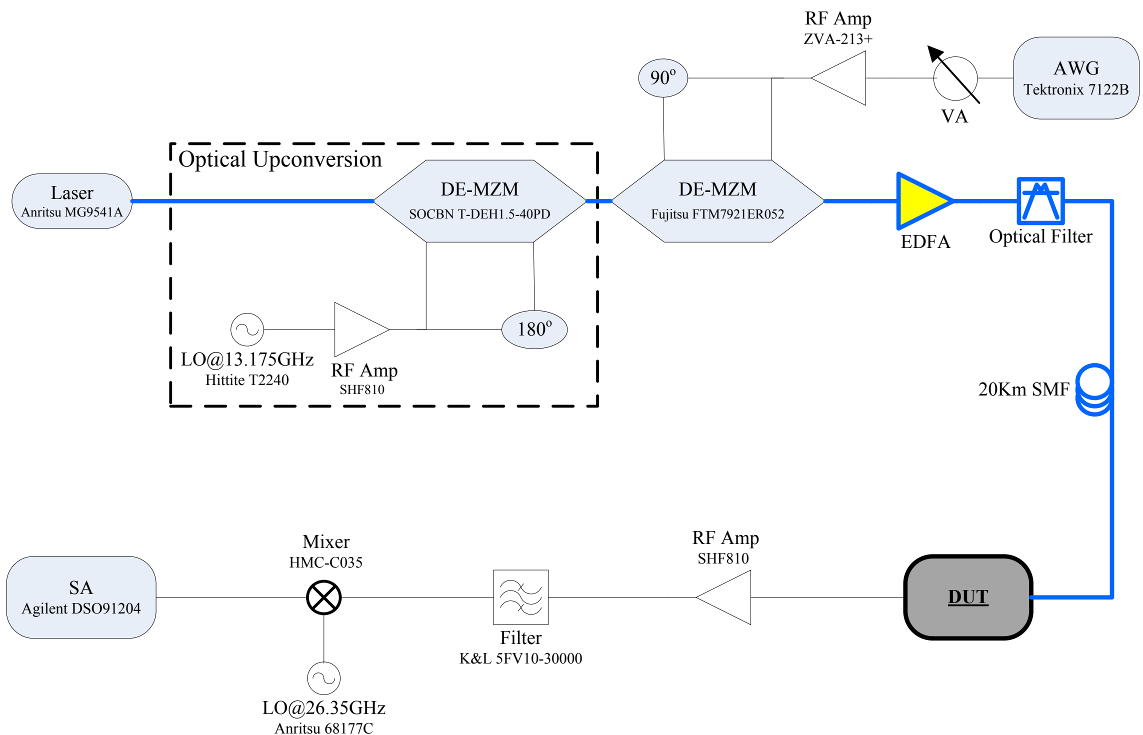

Figure 4.13: Setup for EVM measurement.

Before the optical signal is uploaded to the link, optical amplifier (EDFA) and filter are used to balance the losses after 20 KM of transmission, which is approximately 4 dB. The RF amplifier after DUT is because of the high electrical insertion loss of the mixer (9 dB). Past the amplification, the signal is filtered by a bandpass filter with the center frequency of 30 GHz. Finally, after passing through the mixer with LO at 26.35 GHz, the signal is down-converted from 30.31 GHz back to standard UWB of Band Group#1, centered at 3.96 GHz.

Result

Electrical spectrum of the signal before down-conversion is presented in Figure 4.14. Centered at 30.31 GHz, the average signal-noise-ratio is around 15 dB.

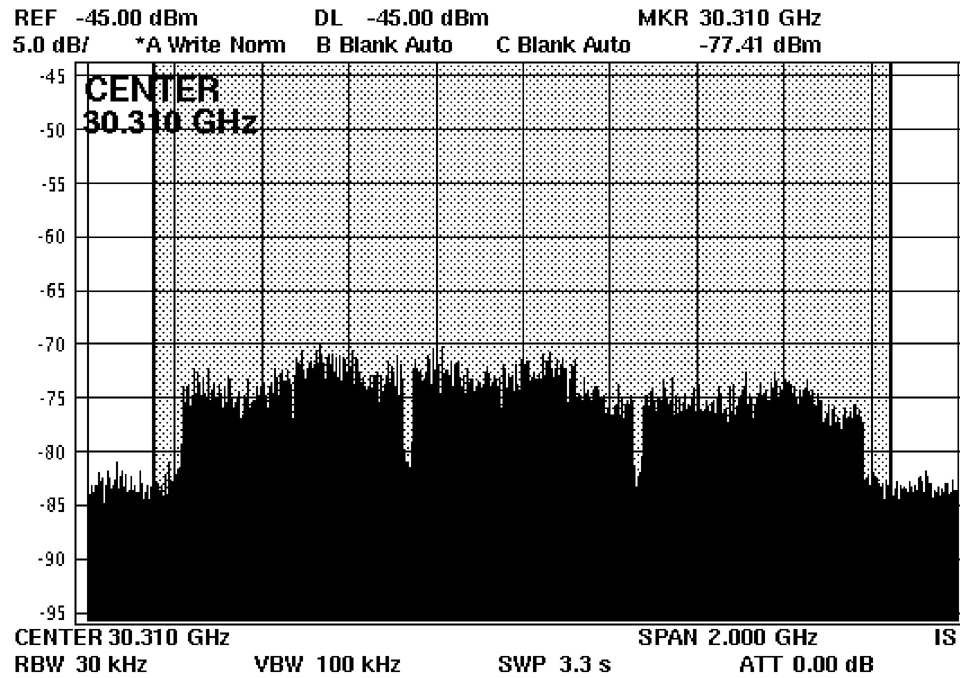

Figure 4.14: Electrical spectrum of up-converted UWB at the optical receiver.

EVM variation versus RF input power is demonstrated in Figure 4.15. According to WiMedia UWB specification [70], at 480 Mbps and with 4 dB of transmission loss, the minimum acceptable EVM value is -18 dB, which corresponds to RF input power from -11.64 dBm to 0 dBm.

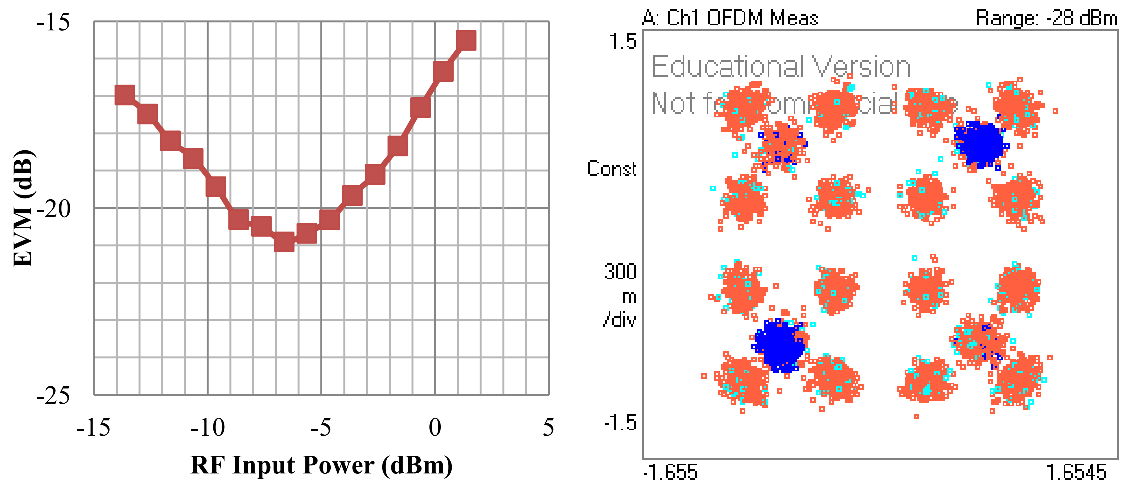

Figure 4.15: RF input power versus EVM (left) and constellation at lowest EVM point (right).

4.3.4 Dynamic Range

Setup

Two types of dynamic range were characterized. The Linear Dynamic Range indicates the maximum RF input power until the circuit output saturates, and it was measured at six different frequencies from a single RF signal generator. The Spurious-Free Dynamic Range (SFDR) shows the connection between received signal and residues created by amplifier nonlinearities and it was characterized with two sets of two-tone signals.

Measurement setting for Linear Dynamic Range is shown in Figure 4.16 and only one RF Source is required. But in SFDR measurement, in order to acquire two-tone signals, the RF input of MZM is connected to the Power Divider which combines the signals from RF Source 1 and RF Source 2, as the arrow in Figure 4.16 shows.

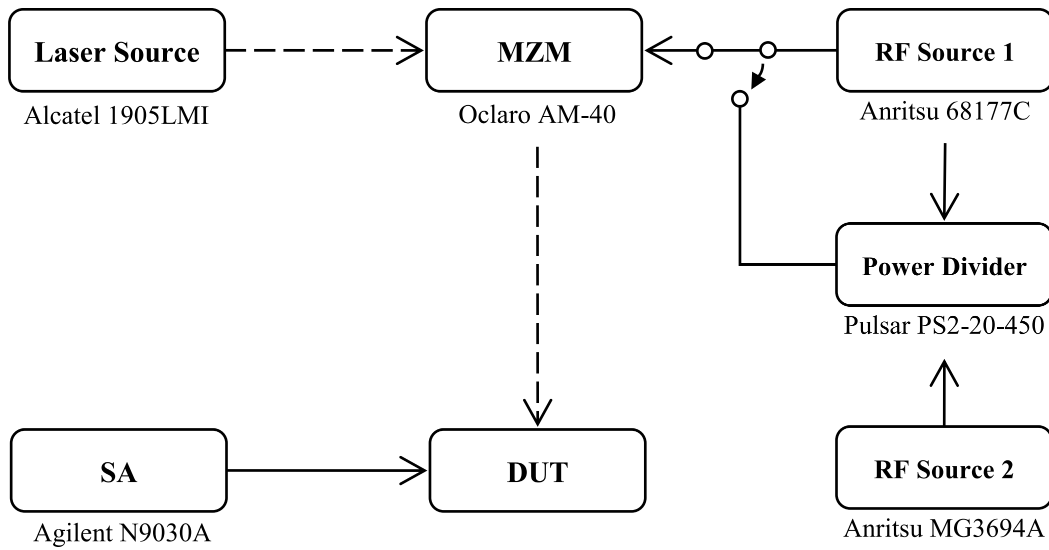

Figure 4.16: Setup for dynamic range measurement.

A note regarding the equipment specification, which is the output power of RF signal generator varies with the frequency, and generally it decreases as the frequency moves up. For Anritsu 68177C, the maximum nominal output power is 20 dBm, but it is reduced to 19 dBm at 10 GHz, 16 dBm at 15 GHz, 14 dBm at 20 GHz, and 11 dBm at 30 GHz.

In SFDR characterization, since the upper frequency limit of power divider is 18 GHz, thus both two-tone signal sets must be within this value. Frequencies chosen for the first set signals are 4 GHz and 6 GHz, and their corresponding Third-order Intermodulation (IMD3) frequencies are 2 GHz and 8 GHz. The second set signals are 13 GHz and 14 GHz, and the corresponding IMD3 are 12 GHz and 15 GHz.

Results

As Figure 4.17 shows, the receiver enters into saturation mode between 10 dBm to 12 dBm of RF input power, depending on the frequency. As previously stated, the maximum power of RF source at 30 GHz is limited to 11 dBm, therefore the gain curve of 30 GHz measurement appears to be flat after this value.

The average 1-dB compression point (referred to input) is identified as 11.7 dBm and its frequency chart is shown in Figure 4.18.

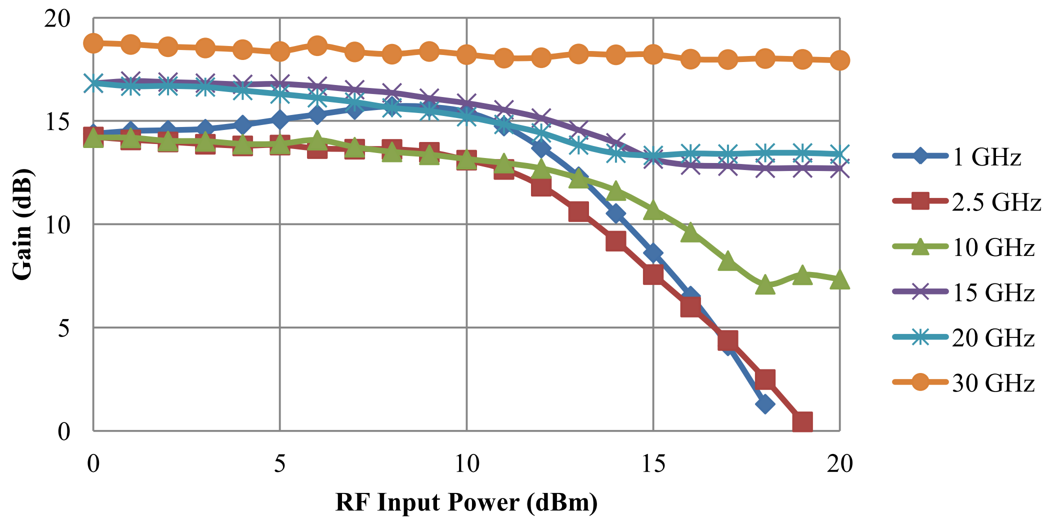

Figure 4.17: RF input power versus output gain at different frequencies.

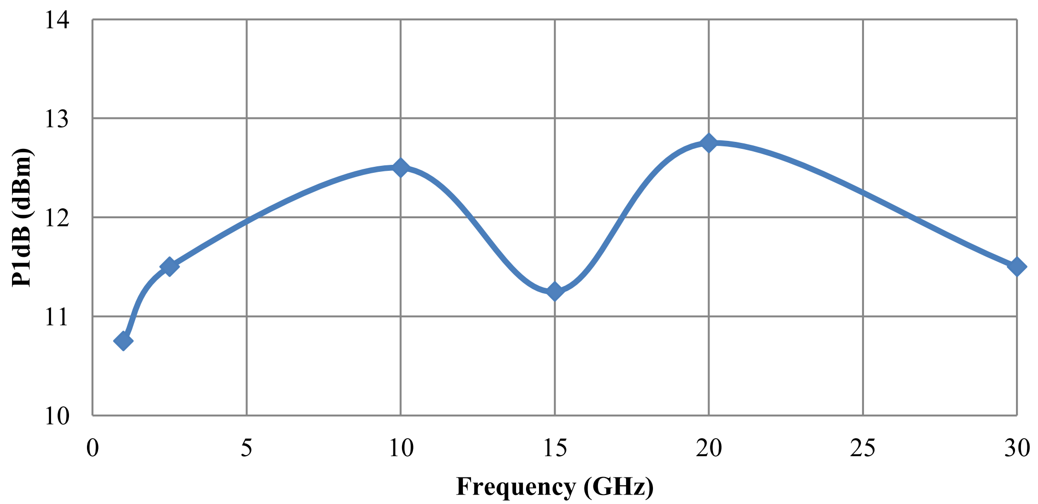

Figure 4.18: 1-dB compression point referred to RF input.

Regarding SFDR, it measures the maximum signal power whereas the third-order product is as low as the system noise level (see Figure 4.19). During the measurement, the noise level detected and normalized to 1 Hz resolution bandwidth is -174.3 dBm/Hz. Values of each tone, including IMD3, were sampled and averaged within 500 ms of time length at 4.7 KHz of resolution bandwidth, and accordingly the SFDR of the first set signals and the second set signals are found as 107.6 dB/Hz$^{2/3}$ (Figure 4.19) and 107.3 dB/Hz$^{2/3}$ (Figure 4.20), respectively.

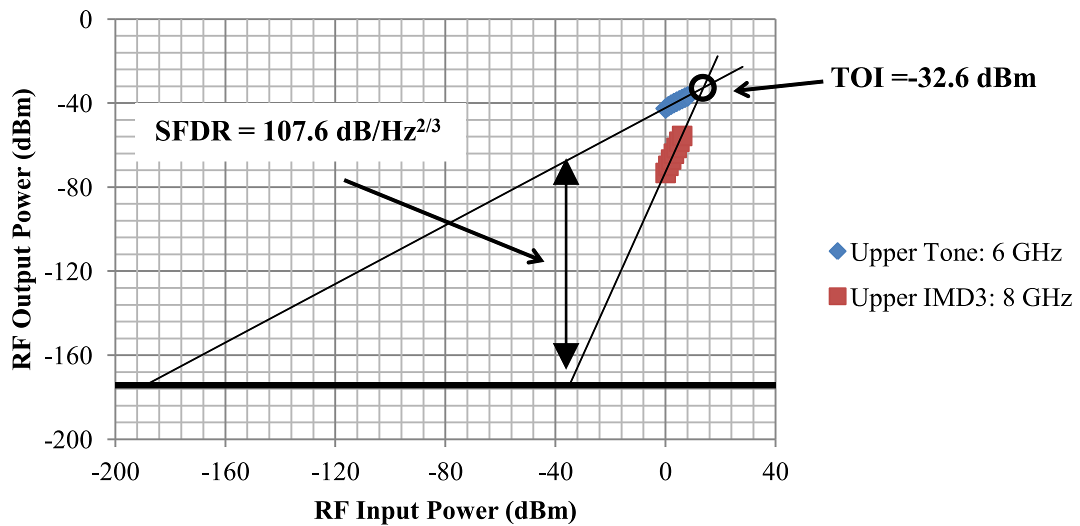

Figure 4.19: SFDR of the first set signal.

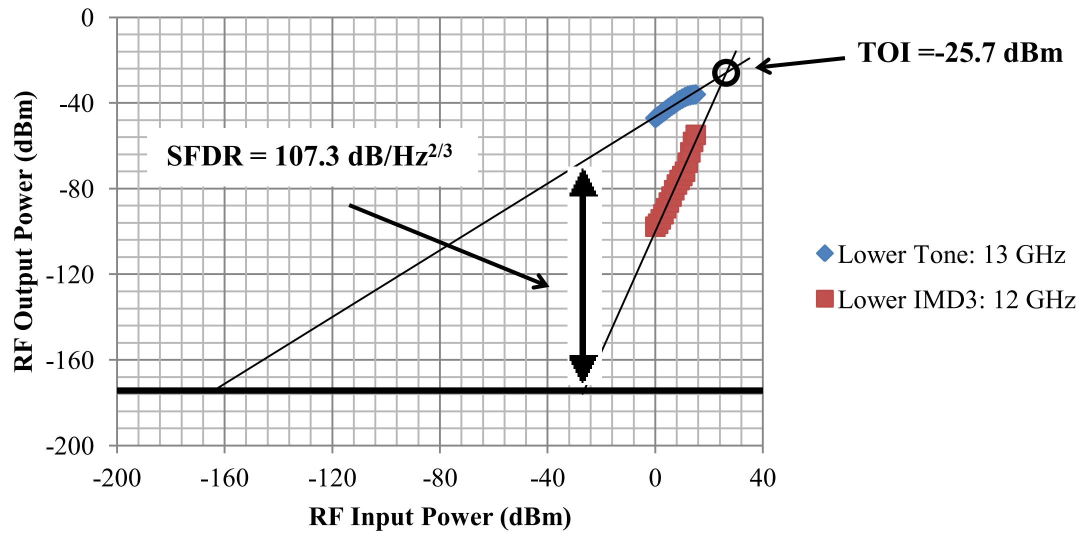

Figure 4.20: SFDR of the second set signal.

Some screenshot examples during SFDR characterization are demonstrated in Figure 4.21 (first set signal) and Figure 4.22 (second set signal). Note the value of each tone was actually acquired under 4.7 KHz of resolution bandwidth and 500 KHz of frequency span, not from the readings displayed on the screenshot.

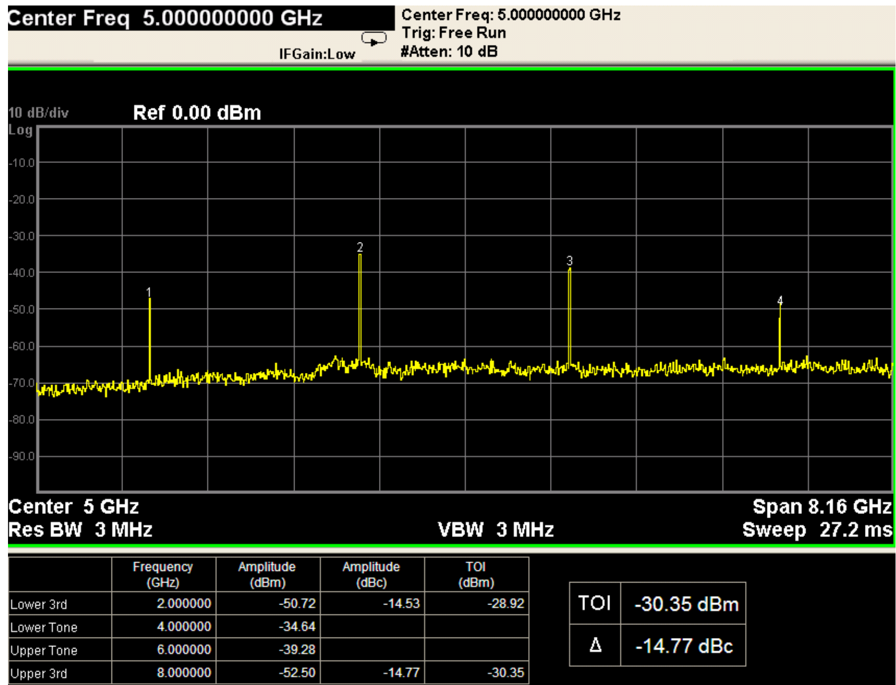

	Frequency (GHz)	Amplitude (dBm)	Amplitude (dBc)	TOI (dBm)
Lower 3rd	2.000000	-50.72	-14.53	-28.92
Lower Tone	4.000000	-34.64		
Upper Tone	6.000000	-39.28		
Upper 3rd	8.000000	-52.50	-14.77	-30.35

Figure 4.21: Output power of the first set signal and IMD3 at 8 dBm of input power.

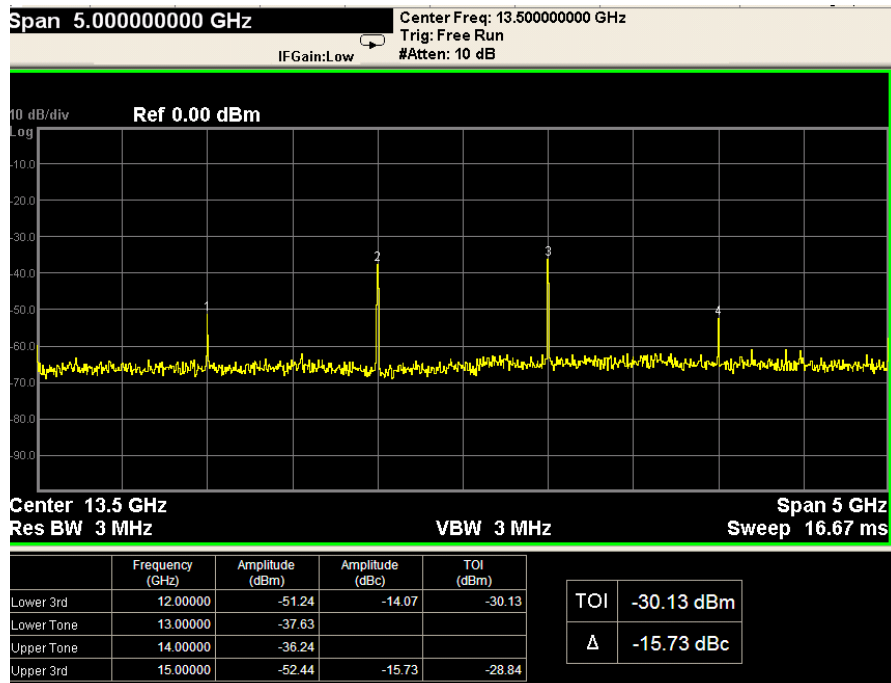

	Frequency (GHz)	Amplitude (dBm)	Amplitude (dBc)	TOI (dBm)
Lower 3rd	12.00000	-51.24	-14.07	-30.13
Lower Tone	13.00000	-37.63		
Upper Tone	14.00000	-36.24		
Upper 3rd	15.00000	-52.44	-15.73	-28.84

Figure 4.22: Output power of the second set signal and IMD3 at 20 dBm of input power.

Still from the SFDR response, we can also derive the Third-Order Intercept (TOI) point (indicated in Figure 4.19) by extending the signal response line and the third-order harmonic response line. TOI value referred to the output is -32.6 dBm for first set and -25.7 dBm for the second set.

4.3.5 Eye-Diagram

Setup

Using a pattern generator to create a pseudo-random bit sequence, the optical receiver was measured at three different bit rates: 12 Gbps, 40 Gbps and 43 Gbps. The measurement setup is indicated in Figure 4.23.

For 40 Gbps and 43 Gbps measurement, an additional RF amplifier from SHF [71] and a 10 dB attenuator are used, providing a combined gain of 10 dB. This additional set is to counteract the electrical loss of MZM, but mainly to provide sufficient signal power on the optical receiver which has known low-performance beyond 30 GHz.

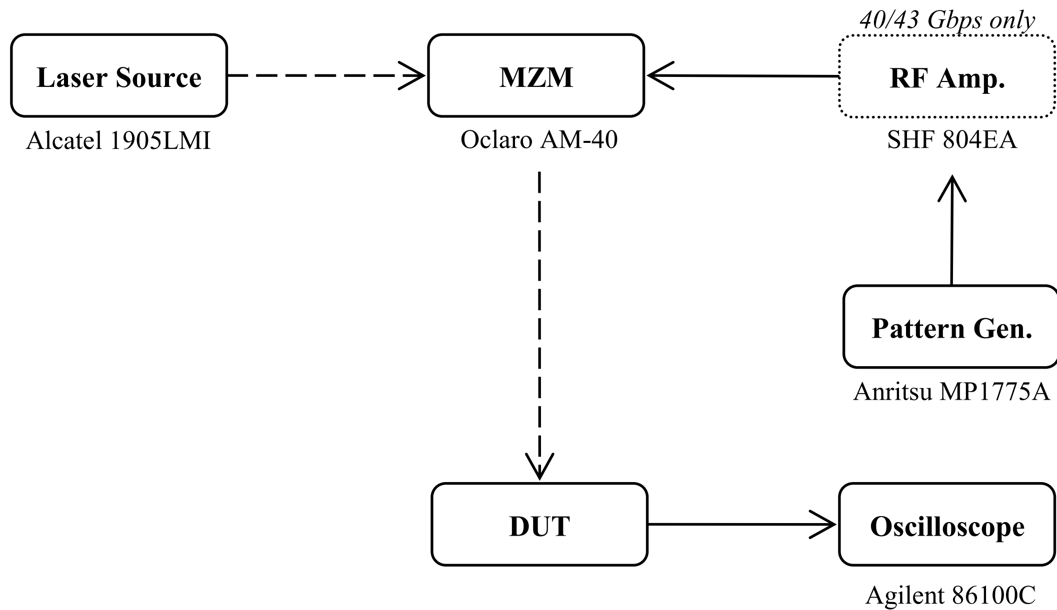

Figure 4.23: Setup for eye-diagram measurement.

Results

At 12 Gbps and 2 V_{p-p} of input voltage, Figure 4.24 shows the average output voltage measured on single-ended port is 64 mV_{p-p} and the Q-factor is 6.2, which is equivalent to BER = 10^{-9}. However, the output voltage swing could be doubled case it is measured differentially, also with lower noise, but the equipment required for differential measurement were not available at the time when experiment was done.

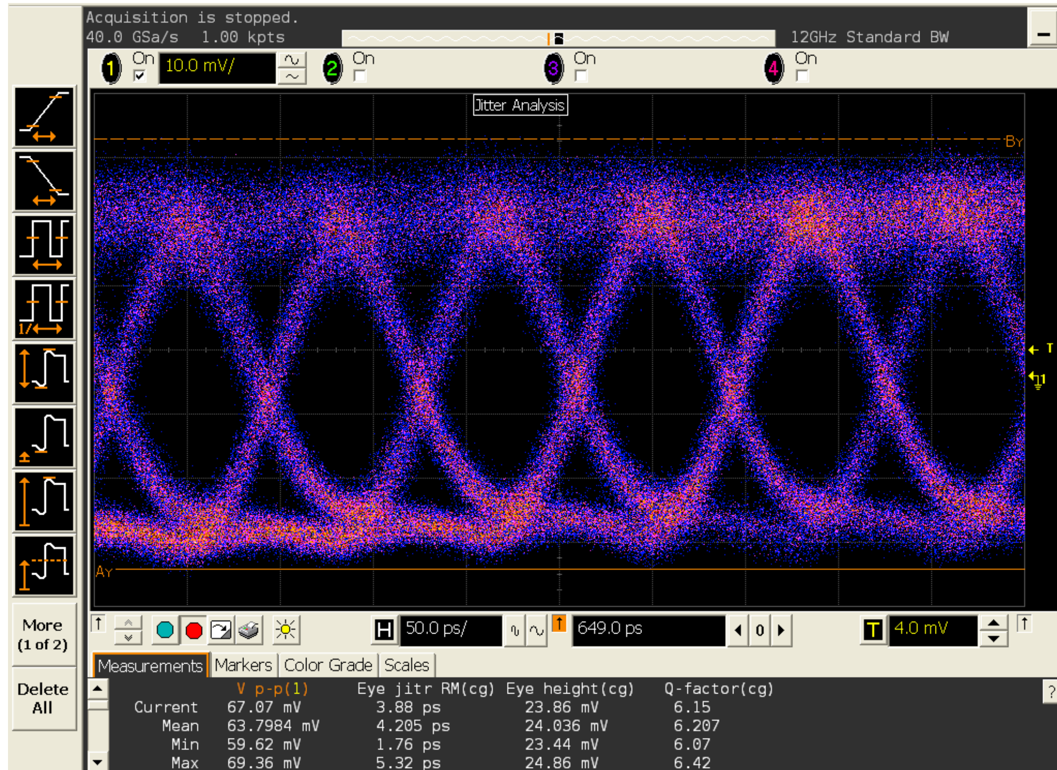

Figure 4.24: Eye-diagram at 12 Gbps.

At 40 Gbps and 1 V_{p-p} of input voltage, readings from Figure 4.25 indicate that output voltage swing has reached 121.6 mV_{p-p} but the Q-factor is reduced to merely 3.71. Certainly the amplitude boost is due to the additional RF amplifier, yet the collective signal degradation caused by bondwire issues on both RF and DC traces, has resulted a noisy signal difficult to identify.

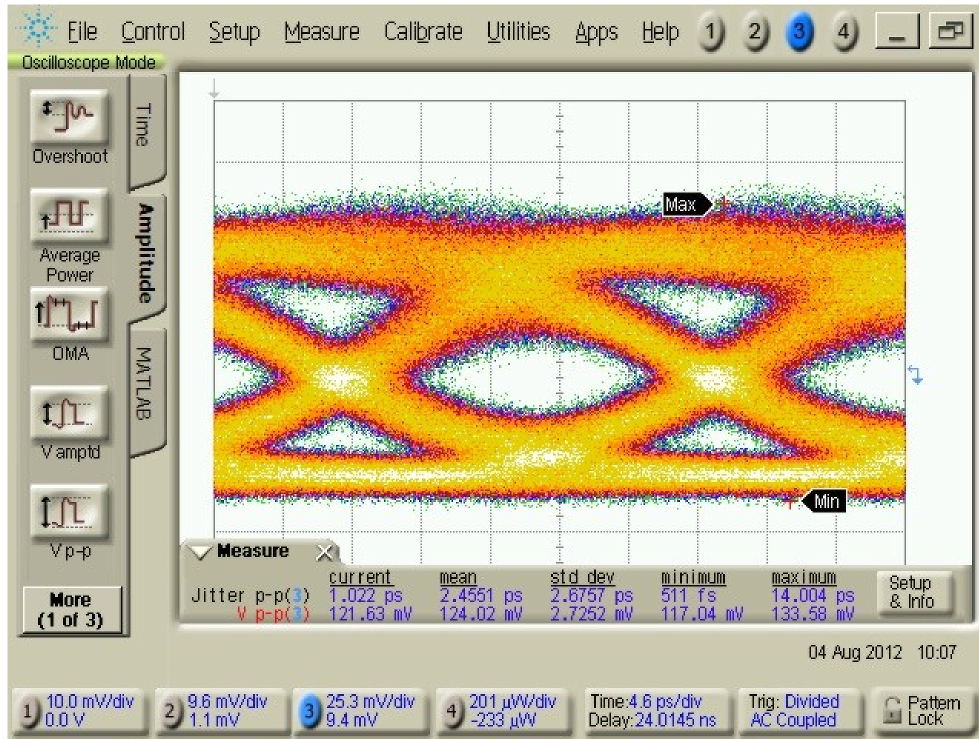

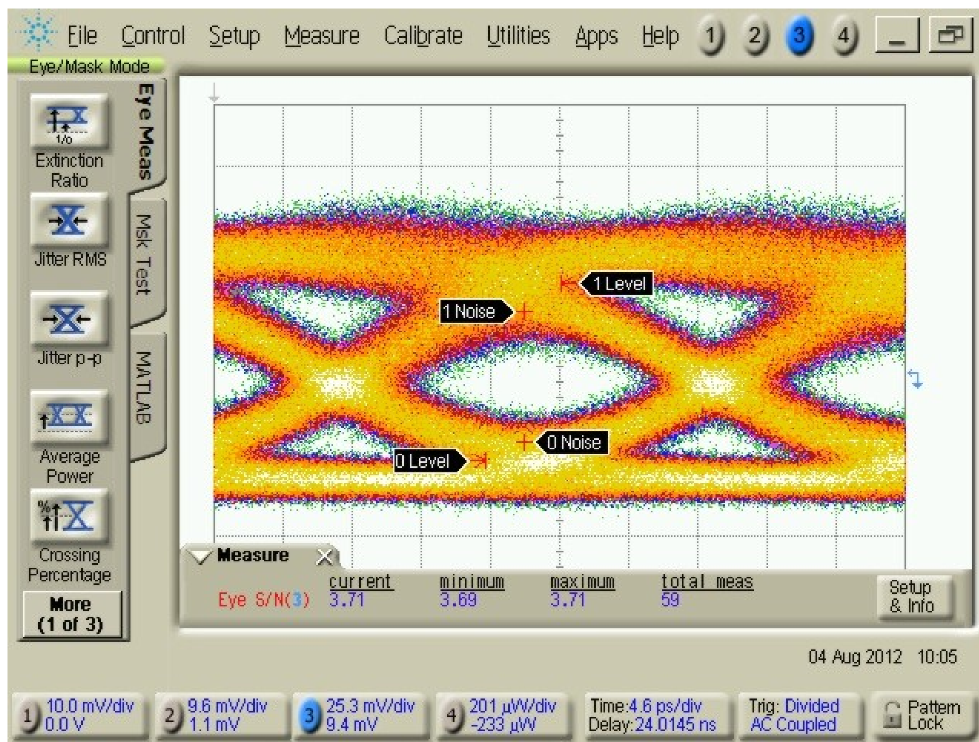

Figure 4.25: Eye-diagram at 40 Gbps.

A tentative measurement at 43 Gbps was also done and shown in Figure 4.26. The output voltage is almost the same but the Q-factor has further degraded to 3.27.

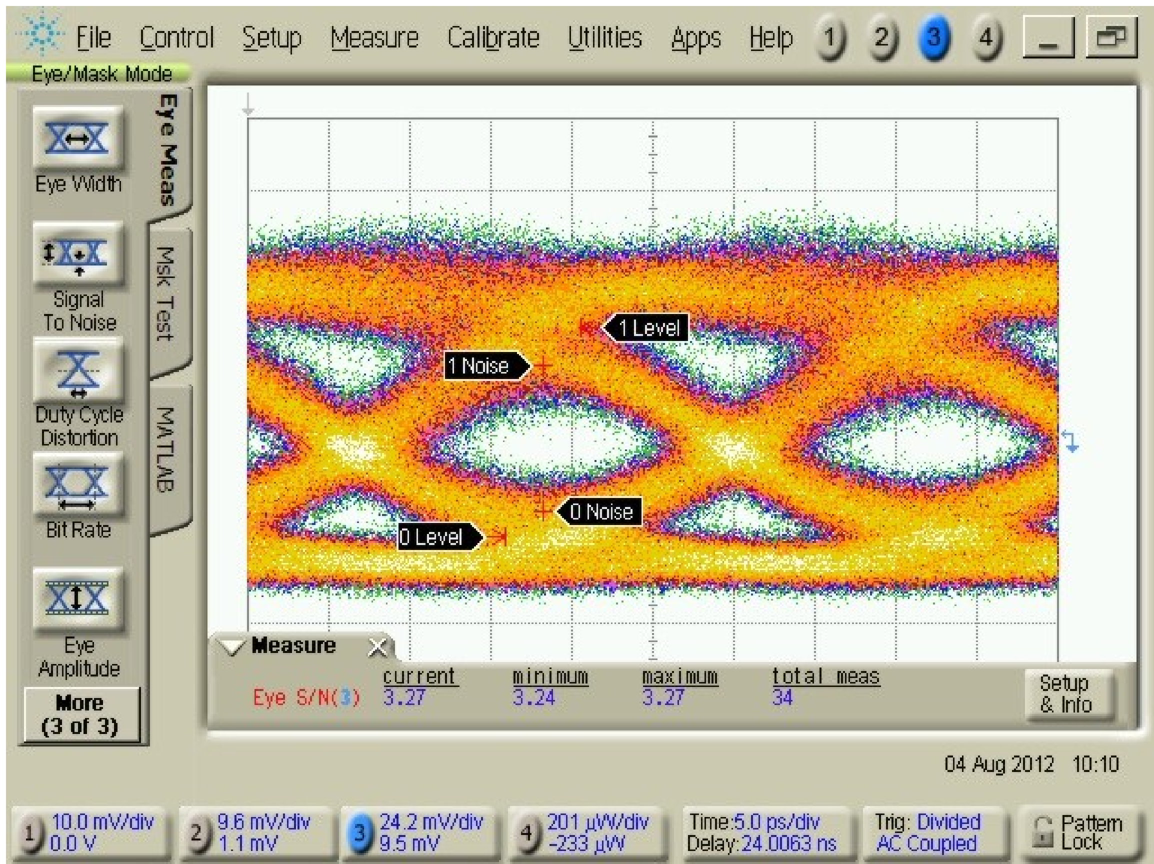

Figure 4.26: Eye-diagram at 43 Gbps.

4.4 Summary

In this chapter, we have discussed the fabrication aspects of the optical receiver and consequences caused by some deviations. First of the four evaluation groups identifies

the responsivity of optical receiver at 1550 nm is 0.325 A/W. Regarding frequency evaluation, the transmission coefficient S_{21} has dropped significantly after 30 GHz and basically the receiver bandwidth is regarded as this value. Bandwidth of 30 GHz is further confirmed by the EVM evaluation, in which a UWB signal is transmitted at 30.31 GHz and processed by our optical receiver. In nonlinearity evaluation, the SFDR of two sets of two-tone signals are found as 107.6 dB/Hz$^{2/3}$ and 107.3 dB/Hz$^{2/3}$. Lastly, in eye-diagram evaluation, the outcome of bondwire effects has also manifested on the signal quality; the Q-factor measured at 12 Gbps is 6.2, equivalent to BER = 10^{-9}, but the receiver has become noisy at 40 Gbps or above, resulting Q-factor no more than 3.7.

CHAPTER 5: CONCLUSION

5.1 Concluding Remarks

The primary goal of this thesis is to implement an ultra-broadband optical receiver for RoF applications, aimed to cover frequency bands from 100 MHz to 50 GHz. The receiver is built in hybrid integrated way which includes a lensed fiber, a photodetector (PD), a transimpedance amplifier (TIA), two bias-tee circuits but later removed, and DC bias circuit.

Unlike most optical receivers, we have used a lensed fiber to replace the conventional fiber-lens method, leading to a much simpler coupling structure. Due to the MFD mismatch between PD and lensed fiber, it is expected to have certain coupling loss even perfect alignment is achieved. Once the optical signal is converted into electrical, the TIA provides current-to-voltage conversion as well as signal amplification. Also, there is a specific demand from TIA which requires bias-tee circuit on each output trace, and this circuit is accomplished with discrete RF components.

Two issues that may impact the receiver performance are mentioned during the design process and simulation, and then verified once the circuit is fabricated. The first problem relates to the optical coupling loss. Loss introduced by MFD mismatch is

already known, but the final result still depends on the alignment precision between fiber and PD. Measurement has shown the total optical coupling loss is -3.91 dB, partly contributed by the epoxy because it has caused the fiber to shift before it being solidified. The second problem involves the bondwires, since their transmission line effects at high frequencies could be significant. For RF signal connections, bondwires were simulated and the result shown they could degrade the overall bandwidth to 26.7 GHz in the worst case. However, this result does not include the effect of bondwire on DC traces, because insufficient bondwires and lengthy connections will add noise to the circuit.

During the back-to-back characterization of optical receiver, average 1-dB compression point sampled at different frequencies is found as 11.7 dBm (referred to input), and the average SFDR based on two sets of two-tone frequencies (4 GHz with 6 GHz, and 13 GHz with 14 GHz) is 107.45 dB/Hz$^{2/3}$. Bandwidth of the optical receiver is identified from S-parameter and EVM measurement, with proven performance of 30 GHz bandwidth. However, due to bondwire effects, operation at 43 Gbps is too noisy according to industrial standards. Therefore, refinement of bondwire implementing method or alternative interconnect solution is expected to be the next step for advancement works. Regarding the optical-to-electrical conversion rate, the receiver

responsivity is found as 0.325 A/W at 1550 nm, which is lower than the nominal PD value 0.8 A/W, because of the MFD mismatch and fiber alignment precision, as stated earlier. This result also points out another possible direction for future work, involving the coupling technique of optical components.

5.2 Future Work

Future works of this thesis can be categorized into three subjects: signal quality, optical coupling technique, and functional upgrades.

Signal Quality

The issue of signal quality starts with the optical insertion loss caused by MFD mismatch. Lensed fiber with smaller MFD is achievable but it was simply unavailable from all companies inquired at the time of circuit fabrication. At least 1 dB of optical loss could be removed if the MFD of lensed fiber and PD are totally matched.

On the electrical side, bondwire is certainly the main problem. Accurate and short bondwire is practicable with higher precision facilities, but unless precise bondwire can

be assured, otherwise flip-chip mounting will be the best solution to avoid signal degradation.

Optical Coupling Technique

The fiber installation process is an interesting subject to be reviewed. In fact, processing details are typically regarded as business confidential, and each company has developed its own technology for maximum coupling efficiency and streamline assembly process. According to a generic report, the use of metalized lensed fiber plus laser welding technique could provide higher-accuracy and more robust attachment comparing to the epoxy that we have used, but it still require further studies to reveal the details. In this work, at least 2.9 dB of optical insertion loss was caused by the fiber-drift after applying the epoxy.

Another topic under this subject is the alignment method. Automatic fiber alignment process would be an interesting target, because conventional methods are inefficient and costly. The basic principle of fiber alignment is to find the best position in three-dimensional space in which the photodetector produces maximum current. It has been reported in [72] the use of dynamic comb-drive actuators integrated in front of the

photodetector receptacle, with a control circuit that adjusts the comb-drive position basing on PD output current, the alignment process is almost automatically completed. But this integration of comb-drive actuators still has some technical difficulties and compatibility issues with the fabrication process, thus structural simplification and less dependent to the fabrication process could be a potential solution to be investigated.

Functional Upgrade

Upgrading the receiver into balanced-photodiode structure will expand its functionality and performance, because this structure will lead to better optical sensitivity, higher dynamic range, and lower noise.

BIBLIOGRAPHY

[1] U.S. Department of Commerce, "United States Frequency Allocations," Oct 2003. [Online]. Available: http://www.ntia.doc.gov/files/ntia/publications/2003-allochrt.pdf. [Accessed Sep 2012].

[2] H. Al-Raweshidy and S. Komaki, Radio over Fiber Technologies for Mobile Communications Networks, Artech House, 2002.

[3] N. Anscombe, "Demand for indoor coverage drives radio-over-fibre, wireless europe," Feb/Mar 2005. [Online]. Available: http://www.nadya-anscombe.com/downloadlibrary/radio%20over%20fibre.pdf. [Accessed 17 Sep 2012].

[4] A. K. Dutta, M. Takechi, R. S. Virk, M. Kobayashi, K. Araki, K. Sata, M. Gentrup and R. Ragle, "40 Gb/s Postamplifier and PIN/Preamplifier Modules for Next Generation Optical Front-End System," *Journal of Lightwave Technology, Vol.20, No.12,* pp. 2229-2238, December 2002.

[5] Y.-H. Kwon, J.-S. Choe, J. Kim, K. Kim, K.-S. Choi, B.-S. Choi and H.-G. Yun, "Fabrication of 40 Gb/s Front-End Optical Receivers Using Spot-Size Converter Integrated Waveguide Photodiodes," *ETRI Journal, Volume 27, Number 5,* pp. 484-489, October 2005.

[6] SHF Communication Technologies AG, "Datasheet: SHF 47100 A, O/E Conversion Module," [Online]. Available: http://www.shf.de/fileadmin/download/47100a.pdf. [Accessed 2 2012].

[7] F. Y. Xu, "High Precision Adhesives for Free Space Micro-Optics Applications," in *Electronic Components and Technology Conference*, 2003.

[8] H. Tsunetsugu, K. Katsura, T. Hayashi, F. Ishitsuka and S. Hata, "A New Packaging Technology Using Microsolfer Bumps for High-Speed Photoreceivers," *IEEE Transactions on Components, Hybrids, and Manufacturing Technology, Vol. 15, No. 4,* pp. 578-582, 1992.

[9] J. H. Song, H. N. J. Fernando, B. Roycroft, B. Corbett and F. H. Peters, "Practical Design of Lensed Fibers for Semiconductor Laser Packaging Using Laser Welding Technique," *Journal of Lightwave Technology, Vol. 27, No. 11,* pp. 1533-1538, 1 June 2009.

[10] J. Chandrappan, Z. Jing, R. V. Mohan, P. O. Gomez, T. A. Aung, Y. Xiao, P. V. Ramana, J. H. Lau and D. L. Kwong, "Optical Coupling Methods for Cost-Effective Polymer Optical Fiber Communication," *IEEE Transactions on Components and Packaging Technologies, Vol. 32, No. 3,* pp. 593-599, September 2009.

[11] Corning Incorporated, "Mode-Field Diameter, Measurement Method," August 2001. [Online]. Available: http://www.corning.com/docs/opticalfiber/mm16_08-01.pdf. [Accessed February 2012].

[12] J. D. Gibson, "Fiber Optic Connectors and Splices," in *The Communications Handbook, 2nd Edition*, CRC Press, 2002, pp. 49-4, 49-5.

[13] D. Wake, T. P. Spooner, S. D. Perrin and I. D. Henning, "50 GHz InGaAs Edge-Coupled pin Photodetector," *Electronics Letters, Vol. 27, No. 12,* pp. 1073-1075, June 1991.

[14] K. Kato, S. Hata, K. Kawano, J. Yoshida and A. Kozen, "High-Efficieny 50 GHz

InGaAs Multimode Waveguide Photodetector," *IEEE Journal of Quantum Electronics, Vol. 28, Issue 12,* pp. 2728-2735, Dec 1992.

[15] E. Sackinger, "P-I-N Photodetector," in *Broadband Circuits for Optical Fiber Communication*, John Wiley & Sons, 2005, pp. 26-27.

[16] J. E. Bowers and J. C. A. Burrus, "Ultrawide-Band Long-Wavelength p-i-n Photodetectors," *Journal of Lightwave Technologies, Vol. 5, Issue 10,* pp. 1339-1350, October 1987.

[17] Archcom Technology Inc., "AC6180-C 40 Gbps Waveguide InP Photodetector," Archcom Technology Inc., Azusa, CA, USA.

[18] A. S. Sedra and K. C. Smith, "Feedback," in *Microelectronic Circuits*, Oxford Press, 2010, pp. 804-890.

[19] E. Sackinger, "Shunt Feedback TIA," in *Broadband Circuits for Optical Fiber Communication*, John Wiley & Sons, 2005, pp. 113-121.

[20] Inphi Corporation, "4335TA - Inphi," [Online]. Available: http://www.inphi.com/products-technology/networking-communications-products/transimpedance-amplifiers/4335ta.php. [Accessed 7 2011].

[21] TriQuint Semiconductor, "TGA4812: 40G Transimpedance Amplifier," TriQuint Semiconductor, May 2009.

[22] RFMD, "SFT-9200B: 50 GHz Transimpedance Amplifier," [Online]. Available: http://www.rfmd.com/CS/Documents/SFT-9200BDS.pdf. [Accessed 4 Sep 2012].

[23] GTRAN, "GTRAN 43 Gbps Transimpedance Amplifier: GT40-5015TA," GTRAN, Camarillo, CA, USA, 2010.

[24] Texas Instruments, "Interfacing Between LVPECL, VML, CML, and LVDS

Levels," December 2002. [Online]. Available: http://www.ti.com/lit/an/slla120/slla120.pdf. [Accessed 19 April 2012].

[25] R. H. Caverly, "Characteristic Impedance of Integrated Circuit Bond Wires," in *IEEE Trans. Microwave Theory Tech., Vol. 34, pp. 982-984*, 1986.

[26] F. Alimenti, U. Goebel and R. Sorrentino, "Quasi Static Analysis of Microstrip Bondwire Interconnections," in *Proc. IEEE MTT-Symp, pp. 679-682*, Orlando, FL, 1995.

[27] T. Krems, W. Haydl, L. Verweyen, M. Schlechtweg, H. Massler and J. Rudiger, "Coplanar Bond Wire Interconnections for Millimeterwave Applications," in *Electrical Performance of Electronic Packaging, pp. 178-180*, 1995.

[28] A. Sutono, N. G. Cafaro, J. Laskar and E. Tentzeris, "Experimental Study and Modeling of Microwave Bond Wire Interconnects," in *IEEE Antennas and Propagation Society International Symposium, Vol. 4, pp. 2020-2023*, Atlanta, GA, 2000.

[29] T. Krems, W. Haydl, H. Massler and J. Rudiger, "Millimeter-wave Performance of Chip Interconnections Using Wire Bonding and Flip Chip," in *IEEE MTT-S Microwave Symposium Digest, Vol. 1, pp. 247-250*, 1996.

[30] K. Mouthaan, "Microwave Modeling and Measurement of the Self- and Mutual Inductance of Coupled Bondwires," in *Bipolar/BiCMOS Circuits and Technology Meeting, pp. 166-169*, 1997.

[31] A. O. Harm, K. Mouthaan, E. Aziz and M. Versleijen, "Modeling and Simulation of Hybrid RF Circtuis Using a Versatile Compact Bondwire Model," in *28th European Microwave Conference, Vol. 2, pp. 529-534*, 1998.

[32] T. P. Budka, "Wide-Bandwidth Millimeter-Wave Bond-Wire Interconnects," *IEEE*

Transactions on Microwave Theory and Techniques, pp. 715-718, Apr 2001.

[33] Y. Miyamoto, M. Yoneyama, Y. Imai, K. Kato and H. Tsunetsugu, "40 Gbit/s Optical Receiver Module Using a Flip-Chip Bonding Technique for Device Interconnection," *Electronics Letters, Vol. 34, Issue 5,* pp. 493-494, 5 May 1998.

[34] E. Camargo, R. S. Virk, R. Haiji, S. Parker, S. Notomi and H. Ohnishi, "Design of broadband amplifier for high speed applications," in *European Microwave Conference*, 2002.

[35] I. Wolff, Coplanar Microwave Integrated Circuits, John Wiley & Sons, 2006.

[36] R. N. Simons, Coplanar Waveguide Circuits, Components, and Systems, John Wiley & Sons, 2001.

[37] S. Marsh, Practical MMIC Design, Artech House, 2006.

[38] M. Houdart, "Coplanar Lines: Application to Lumped and Semi-Lumped Microwave Integrated Circuits," in *7th European Microwave Conference, pp.450-454*, 1977.

[39] R. Sorrentino and G. Bianchi, "Basic MMIC elements," in *Microwave and RF Engineering*, John Wiley & Sons, 2010, pp. 640-641.

[40] T. Becks and I. Wolff, "Full-Wave Analysis of Various Coplanar Bends and T-Juntions with Respect to Different Types of Air-Bridges," in *Microwave Symposium Digest, Vol.2, pp.697-700*, 1993.

[41] H. Kim and R. Franklin-Drayton, "Wire-Bond Free Technique for Right-Angle Coplanar Waveguide Bend Structures," *IEEE Transactions on Microwave Theory and Techniques, Vol.57, No. 2,* pp. 442-448, February 2009.

[42] K. C. Gupta, R. Garg, I. Bahl and P. Bhartia, "Microstrip Applications," in

Microstrip Lines and Slotlines, Artech House, 1996, pp. 122-152.

[43] B. C. Wadell, "Inductors & Capacitors," in *Transmission Line Design Handbook*, Artech House, 1991, pp. 379-431.

[44] I. Wolff, "Coplanar Lumped Elements," in *Coplanar Microwave Integrated Circuits*, John Wiley & Sons, 2006, pp. 249-304.

[45] Poly-GRAMES Research Center, "RF Circuit Fabrication Rules," [Online]. Available: http://132.207.65.61/pcb-process/RF_circuit_fabrication_rules.pdf. [Accessed Feb 2012].

[46] "Bias Network," in *Practical Microstrip Design and Applications*, Artech House, 2005, pp. 288-291.

[47] R. K. Joshi, "Characteristics of a Rotated Butterfly Radial Stub," in *Microwave Symposium Digest, IEEE MTT-S, pp.1165-1168*, 2006.

[48] M. S. Razalli, "Compact "Butterfly" Microwave Ultra-Wideband Filter," in *Asia-Pacific Conference on Applied Electromagnetics, pp.1-5*, 2007.

[49] D. Zhihong, "A 40GHz Amplifier Design Using CPW," in *International Symposium on Electromagnetic Compatibility, pp.337-340*, 2007.

[50] K.-S. Choi, Y.-H. Kwon, J.-S. Choe, Y.-D. Chung, Y.-S. Kang, J. Kim, B.-T. Ahn and J.-T. Moon, "Development of Packaging Technologies for High-Speed (>40Gb/s) Optical Modules," *IEEE Journal of Selected Topics in Quantum Electronics, Vol.12, Issue 5,* pp. 1017-1024, 2006.

[51] H.-G. Yun, K.-S. Choi, Y.-H. Kwon, J.-S. Choe and J.-T. Moon, "Integration and Characteristics of 40-Gb/s Electroabsorption Modulator Integrated Laser Module with a Driver Amplifier and Bias Tees," *IEEE Transactions on Advanced*

Packaging, Vol.31, Issue 4, pp. 855-860, Nov 2008.

[52] R. N. Simons, "Coplanar Waveguide Spiral Inductor," in *Coplanar Waveguide Circuits, Components, and Systems*, John Wiley & Sons, 2001, pp. 262-266.

[53] I. Wolff, "The Coplanar Spiral Inductor," in *Coplanar Microwave Integrated Circuits*, John Wiley & Sons, 2006, pp. 276-295.

[54] N. Kinayman and M. I. Aksun, "Microwave Lumped Elements," in *Modern Microwave Circuits*, Artech House, 2005, pp. 533-544.

[55] N. Masoumi, S. Safavi-Naeini and M. Elmasry, "An Efficient and Accurate Model for RF/Microwave Spiral Inductors Using Microstrip Lines Theory," in *International Conference on Computer Design, pp.127-132*, 2000.

[56] J. Y. Hasani, M. Kamarei and F. Ndagijimana, "Inductor Design and Optimization for Millimeter Wave Integrated Circuit Applications," in *IEEE 18th International Symposium on Personal, Indoor and Mobile Radio Communications, pp.1-4*, 2007.

[57] J. Brinkhoff, K. Koh, K. Kang and F. Lin, "Scalable Transmission Line and Inductor Models for CMOS Millimeter-Wave Design," in *IEEE Transactions on Microwave Theory and Techniques, Vol. 56, Issue 12, pp.2954-2962*, 2008.

[58] D. Dubuc, T. Tournier, I. Telliez, T. Parra, C. Boulanger and J. Graffeuil, "High Quality Factor and High Self-Resonant Frequency Monolithic Inductor for Millimeter-Wave Si-based IC's," in *IEEE MTT-S International Microwave Symposium Digest, Vol.1, pp.193-196*, 2002.

[59] J. Shi, K. Kang, Y. Z. Xiong, J. Brinkoff, F. Lin and X.-J. Yuan, "Millimeter-Wave Passives in 45-nm Digital CMOS," *IEEE Electron Device Letters, Vol. 31, Issue 10,* pp. 1080-1082, 2010.

[60] C.-Y. Chi and G. M. Rebeiz, "Planar millimeter-wave microstrip lumped elements using micro-machining techniques," in *IEEE MTT-S, International Microwave Symposium Digest, Vol.2, pp.657-660*, 1994.

[61] Coilcraft Inc., "Coilcraft: Rugged, Surface Mount Broadband Conical Inductors," [Online]. Available: http://www.coilcraft.com/pdfs/bcr.pdf. [Accessed May 2012].

[62] AVX Corporation, "AVX: GX02 Series FFVS Data Sheet," [Online]. Available: www.avx.com/docs/catalogs/gx.pdf. [Accessed May 2012].

[63] H. Patterson, "Analysis of ground bond wire arrays for RFICs," in *IEEE MTT-S International Microwave Symposium Digest*, Tempe, AZ, 1997.

[64] SHF Communication Technologies AG, "Precision Coaxial Connectors," [Online]. Available: http://www.shf.de/fileadmin/download/Connectors_and_Cables/kmco_complete_v004.pdf. [Accessed 19 June 2012].

[65] Coorstek Inc., "Thin Film Substrates," [Online]. Available: http://www.coorstek.com/resources/8510-1164ThinFilm.pdf. [Accessed 29 June 2012].

[66] Picosecond Pulse Labs, "Bias Tees: Model 5542," [Online]. Available: http://www.picosecond.com/product/product.asp?prod_id=27. [Accessed 7 Aug 2012].

[67] u2t Photonics AG, "XPDV4120R," [Online]. Available: http://www.u2t.com/index.php/products/photodetectors/item/xpdv4120r?category_id=2. [Accessed 8 Aug 2012].

[68] Alcatel Optronics, "Alcatel 1905 LMI," 2002. [Online]. Available: http://pdf.dzsc.com/autoupload/230600db-8d02-444f-b336-ca659ebba386.pdf.

[Accessed 5 Aug 2012].

[69] Oclaro, "PowerLog AM-40," 2009. [Online]. Available: http://www.oclaro.com/datasheets/Oclaro_PowerLog_AM2040_v1_1.pdf. [Accessed 5 Aug 2012].

[70] WiMedia Alliance, "WiMedia SER PHY Specification," WiMedia Alliance, 2005.

[71] SHF Communication Technologies AG, "Datasheet: SHF 804 EA Broadband Amplifier," 24 Mar 2004. [Online]. Available: http://www.shf.de/fileadmin/download/804ea.pdf. [Accessed 11 Sep 2012].

[72] B. Morgan, J. McGee and R. Ghodssi, "Automated Two-Axes Optical Fiber Alignment Using Grayscale Technology," *Journal of Microelectromechanical Systems, Vol. 16, No. 1,* pp. 102-110, Feb 2007.